small method
www.small-methods.com

Perovskite Solar Absorbers: Materials by Design

Qiaoling Xu, Dongwen Yang, Jian Lv, Yi-Yang Sun, and Lijun Zhang**

Solar-cell materials with a tetrahedral diamond structure and its derived structures (i.e., zinc blende and chalcopyrite) are the most successful family of materials, with power conversion efficiencies exceeding 20%. Recent breakthroughs based on lead halide perovskites have inspired intensive research on low-cost photovoltaics beyond diamond-structured materials. While research has focused on addressing the key challenges faced by lead halide perovskites, that is, the stability and toxicity issues, it is of greater interest to develop perovskites into a new family of solar-cell materials. Here, the recent efforts toward this goal are reviewed. The focus is on computational materials design, including single, double, 2D, and nonhalide perovskites and perovskite-like materials. Meanwhile, related experiments are also reviewed with a hope that such this will help identify potential issues as well as enlightening ideas to achieve further computation-driven materials discovery.

1. Introduction

Utilizing solar energy to generate electricity through the photovoltaic (PV) effect is a promising technology that can potentially eliminate the use of the limited amount of fossil fuels. The current PV industry is predominately silicon-based with a small share contributed by CdTe and $Cu(In,Ga)Se_2$ (or CIGS). While the total global installed capacity of PV has reached 300 GW as of 2016,[1] the supply of solar-grade single/polycrystalline silicon has always been a concern when the production is scaled up toward the 30 TW level to make PV a major energy source. A similar material supply issue exists for CdTe and CIGS, as both of these materials contain rare elements. The search for alternative solar-cell materials has thus been a main thrust of renewable energy research worldwide.

Dr. Q. Xu, Dr. D. Yang, Dr. J. Lv, Prof. L. Zhang
Key Laboratory of Automobile Materials of MOE
and College of Materials Science and Engineering
Jilin University
Changchun 130012, China
E-mail: lijun_zhang@jlu.edu.cn
Prof. Y.-Y. Sun
State Key Laboratory of High Performance Ceramics
and Superfine Microstructure
Shanghai Institute of Ceramics
Chinese Academy of Sciences
Shanghai 201899, China
E-mail: yysun@mail.sic.ac.cn
Prof. L. Zhang
State Key Laboratory of Superhard Materials
Jilin University
Changchun 130012, China
The ORCID identification number(s) for the author(s) of this article can be found under https://doi.org/10.1002/smtd.201700316.

DOI: 10.1002/smtd.201700316

The past several years have witnessed a phenomenal growth of research on perovskite solar-cell materials.[2–14] The power conversion efficiencies (PCEs) of perovskite solar cells have exceeded 22%,[15] on par with other conventional commercialized thin-film solar cells.[16] This breakthrough sets the onset of the successful use of nontraditional semiconductors in PV. Thus far, high efficiencies have been achieved using organic–inorganic hybrid halide perovskites, as represented by $CH_3NH_3PbI_3$. Mixing of formamidinium (FA) or Cs at the CH_3NH_3 (methylammonium or MA) cation sites and mixing Br or Cl at the I anion sites have been commonly adopted to improve the efficiency.[15,17–25] The high PV performance results from the fact that this class of materials satisfies almost all the requirements for best-performance PV applications, as listed in **Table 1**. The success of halide perovskites has ignited a wave of search for other perovskite solar-cell materials.[6,14,26–31] The motivation of this search is twofold: on one hand, the current halide perovskites suffer from two critical problems toward practical applications, namely, the instability in a humid environment or under solar irradiation and toxicity due to the use of lead.[32] On the other hand, there is a hope to discover new solar-cell materials inspired by halide perovskites. As the family of tetrahedral semiconductors of Si, CdTe, and CIGS is derived from the diamond structure, a new family of perovskite-derived solar materials is expected to develop, which holds great promise for low-cost PV technology.

There have been excellent reviews from the aspects of understanding materials physics and improving the device efficiency for halide perovskites.[2–5,7–10] This review will focus on new materials by design aiming at solving the technical barriers to solar-cell commercialization faced by halide perovskites. While we will mainly summarize the literature on computational works, for the sake of being coherent, we will discuss the experiments directly or indirectly related to the computations as well. We hope such an intertwined review on both theory and experiment will help identify potential issues underlying the materials design research as well as enlighten ideas to further computation-driven materials discovery. Since the first synthesis of $MAPbI_3$ and the corresponding bromide and chloride materials,[33,34] there have been scattered computational studies on these materials.[35,36] Targeted materials design, however, started only when a reasonably high efficiency was achieved by $MAPbI_3$ and when the technical issues were widely recognized. The most widely practiced materials design in this field is elemental substitution/composition

Table 1. Summarized requirements for the best-performance PV applications in terms of materials and properties categories.

Categories		Requirements
Properties	①	Suitable bandgap matching the solar spectrum
	②	Strong absorption coefficient
	③	Good and balanced carrier mobility
	④	Defect tolerant
	⑤	Ambipolar dopability
	⑥	Long carrier lifetime and diffusion length
	⑦	Reasonably low exciton binding
Materials	⑧	Earth abundant/low cost
	⑨	Nontoxic
	⑩	Long-term stability

engineering in normal single perovskites, which has been used in experiments to enhance both the efficiency and stability of solar cells.[15,18–20,22–25,37–42] Such semiconductor alloys, however, have rarely been studied theoretically, partly due to the complexity of handling alloys by most periodicity-based computational methods. The "materials by design" approach has also been applied to heterovalent substitution in double perovskites, 2D Ruddlesden–Popper perovskites and other perovskite-like materials. We will review the progress on these materials, including the most widely studied halides and newly emerging chalcogenides; for completeness, we will also review the traditional oxide perovskites with ferroelectricity targeting at PV applications, as summarized in **Figure 1**. **Table 2** summarizes the advantages and disadvantages of the materials, properties, and devices for various types of perovskite solar absorbers.

2. Halide Perovskites

2.1. Basic Properties and Problems of Halide Perovskites

Prototypical single halide perovskites have the formula of AMX_3, where the A site is a monovalent inorganic/organic cation (e.g., Cs^+, MA^+, or FA^+), M is a divalent cation (e.g., Pb^{2+}, Sn^{2+}, or Ge^{2+}), and the X site is a halogen anion (e.g., I^-, Br^-, or Cl^-). The perovskite structure, as shown in **Figure 2**a, can be viewed as a 3D framework of corner-sharing $[MX_6]$ octahedra with A-site cations occupying the body-centered hollow sites to stabilize the $[MX_6]$ framework. While the M-site cations are sixfold coordinated by X anions, the A-site cations are 12-fold coordinated by X anions.

The stability of the perovskite structure can usually be described by two empirical parameters, namely, Goldschmidt's tolerance factor, $t = \frac{(r_A + r_X)}{\sqrt{2}(r_M + r_X)}$, and the octahedral factor, $\mu = \frac{r_M}{r_X}$, where r_A, r_M, and r_X are the ionic radii of the A-site, M-site, and X-site ions, respectively. For inorganic AMX_3 halides, a previous statistical analysis indicated that the stabilization of the perovskite structure requires $0.81 < t < 1.11$[71] and $0.44 < \mu < 0.90$.[71] Under ideal conditions, maintaining a high-symmetry cubic perovskite structure requires that the tolerance factor t should be close to 1. At elevated temperature, a cubic perovskite structure (α phase) may exist when t lies between 0.89 and 1. In general, a smaller t between 0.71 and 0.89 could lead to lower-symmetry β (tetragonal) or γ (orthorhombic) phases containing distorted and tilted $[MX_6]$ octahedra. If t is less than 0.71, the perovskite structure cannot be formed. When t is significantly greater than 1, the 3D $[MX_6]$ framework becomes unstable, leading to the formation of a 2D layered structure. According to the definition of t, the ionic radius of the A-site cation must be larger than that of the M-site cation to ensure t is close to 1. Even though Cs^+ has the largest ionic radius across the periodic table, excluding radiative elements, it is still not large enough to form a stable cubic perovskite (e.g., with a t of ≈0.85 when the M site is occupied by Pb): the cubic phase of $CsPbI_3$ is not stable and tends to transform into the wide-gap yellow orthorhombic phase with edge-sharing octahedra.[72] The photoactive cubic phase can only be obtained at temperatures higher than 583 K.[72] To stabilize the cubic perovskite structure,

Yi-Yang Sun received his Ph.D. degree from National University of Singapore (NUS) in 2004. Since then, he has worked as postdoc at NUS, National Renewable Energy Laboratory, and Rensselaer Polytechnic Institute (RPI). In 2010, he was appointed research assistant professor and later research scientist at RPI. In 2017, he assumed a professor position at Shanghai Institute of Ceramics, Chinese Academy of Sciences. His research interest is on the study of energy-related materials using first-principles computations. His current focus is on the design of novel solar-cell materials, in particular, perovskite and other ionic semiconductors.

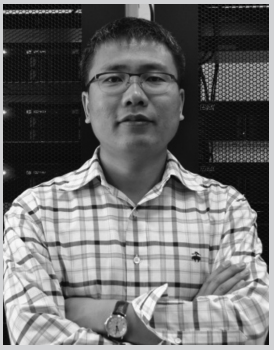

Lijun Zhang obtained his B.S. degree at Northeast Normal University (2003), and completed his Ph.D. with Prof. Yanming Ma and Prof. Guangtian Zou at Jilin University (2008). As a postdoctoral researcher, he joined Prof. David J. Singh's group at Oak Ridge National Laboratory (2008), and moved to Prof. Alex Zunger's group at National Renewable Energy Laboratory (2010). He then became a research assistant professor at the University of Colorado at Boulder (2013). In September 2014, he joined Jilin University as a professor. His current interests focus on materials by design and band structures engineering of functional semiconductor materials for optoelectronic applications.

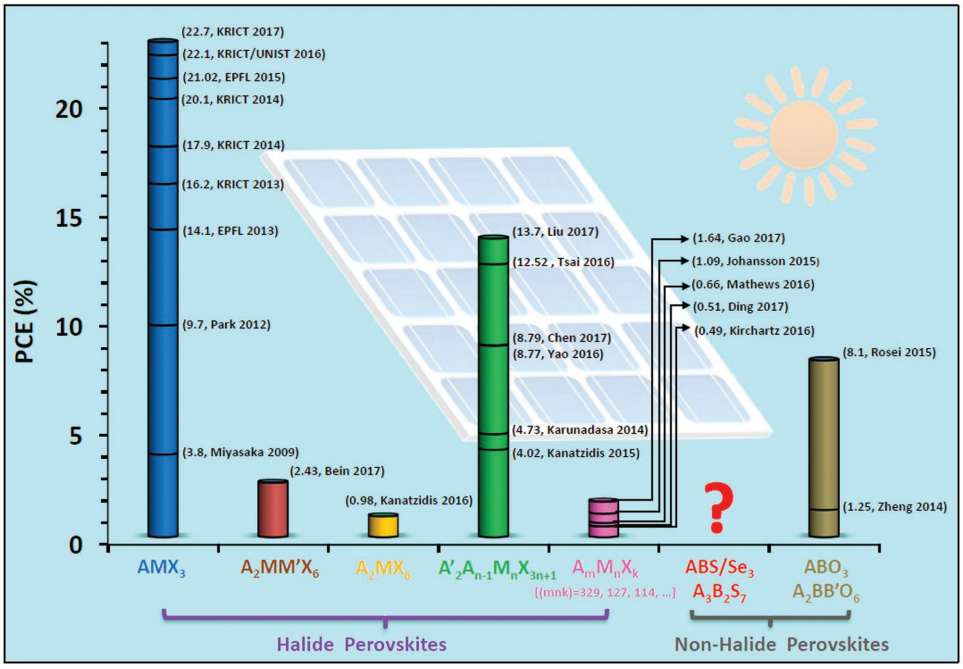

Figure 1. Summary of different perovskite solar absorbers and their representative power conversion efficiencies (PCEs) achieved in solar cells. The data were gathered from refs. [16,28,31,43–55] for the halide perovskites and refs. [56,57] for the nonhalide perovskites.

the A-site cation must be replaced with a larger molecular cation (e.g., MA^+ or FA^+). At room temperature, $MAPbI_3$ adopts a tetragonal β phase; the phase transformations from the tetragonal β phase to the cubic α and orthorhombic γ phases occurs at 330 and 160 K,[58,73] respectively. The MA cations in $MAPbI_3$ can nearly freely rotate at room temperature or higher temperature. As the temperature lowers, the rotation of the MA cations is hindered, and their dipole moments become directional.[74] As seen in the electronic band structure of α-phase $MAPbI_3$ calculated by first-principles density functional theory (DFT) (Figure 2b),[67] the MA cation-derived states are far from the band edges. Intuitively, such an electronic structure suggests that the main role of the MA cations is to function as an electrostatic charge compensator and stabilize the ionic perovskite framework. However, the broken structure symmetry induced by such nonspherical MA cations, accompanied by strong spin–orbit coupling (SOC) of Pb, results in considerable Rashba splitting of the band edges, as indicated by DFT calculations.[75] This is expected to increase the carrier lifetime, as the lowest-energy valence-to-conduction band transition is spin-forbidden. Additionally, it is worth mentioning that a recent experiment demonstrated that the dynamic orientation of the MA cations could screen the excitons and improve the quantum efficiency.[76]

The cubic phase of $MAPbI_3$ has a direct bandgap located at the R point in the Brillouin zone (see Figure 2b). The cubic-to-tetragonal transition with decreasing temperature folds the band edges from R to the zone center (Γ point).[10] According to standard DFT calculations, the dispersion near the band edges results in relatively small effective masses of 0.32 m_0 and 0.36 m_0 (where m_0 is the free electron mass) for electrons and holes, respectively.[77] It has been noted that inclusion of the SOC effect could significantly reduce the calculated effective masses with a smallest reported electron effective mass of 0.08 m_0,[78] comparable to the case of the best solar absorber GaAs.[79] A unique property of $MAPbI_3$ among other solar absorber materials is its balanced effective masses of electrons and holes, which give rise to ambipolar carrier conduction and enables a p–i–n junction solar-cell structure.[6,9,10]

The measured bandgap of $MAPbI_3$ in experiments is ≈1.5 eV,[43,58] close to the optimal bandgap of 1.34 eV of an ideal solar absorber in a single-junction cell. The calculated gap using the high-level GW method including the SOC effect shows reasonable agreement with experiments.[80] The conduction band minimum (CBM) is mainly composed of Pb 6p orbitals (weakly bonding with I 5p orbitals), while the valence band maximum (VBM) is mainly composed of the antibonding hybridized states between Pb 6s and I 5p orbitals. The band-edge wavefunctions shown in Figure 2c suggest isotropic electron and hole transport behavior.[68] The valence-to-conduction band transition from mixed (Pb s, I p) to Pb p orbitals has a high probability, as the result of both high joint density of states (DOS) for the I p to Pb p transition and the intra-atomic Pb s to Pb p transition. This leads to strong optical absorption for $MAPbI_3$. The calculated absorption coefficients of $MAPbI_3$, $CsSnI_3$, and GaAs are shown in Figure 2d.[69] One can see that the optical absorption coefficient of $MAPbI_3$ is up to an order of magnitude higher than that of GaAs within the visible-light region. The high absorption allows a much thinner absorber layer (0.3 µm for cells with 21% PCE)[81] than that in other high-efficiency thin-film solar cells (e.g., GaAs, CdTe, and CIGS), which is typically 2 µm or thicker.[82]

The large dielectric constant of $MAPbI_3$[59,60] resulted from the soft lattice and the enhanced Born effective charge[83] also

Table 2. Advantages and disadvantages of various types of perovskite solar absorbers in terms of material, property, and device aspects.

Perovskite absorbers		Material	Property	Device
Halide perovskites	Single perovskites (AMX_3)	☑ Relatively earth abundant ☑ Low-cost synthesis ☒ Containing toxic lead ☒ Thermodynamic instability	☑ Suitable bandgaps of ≈1.5 eV[43,58] ☑ High threshold light absorption; small carrier effective masses: < 1.0 m_0 ☑ Low exciton binding energy: 2–50 meV[59–61] ☑ Long carrier-diffusion length: > 1 μm[62] ☑ Reasonable carrier mobility: 8–35 $cm^2 V^{-1} s^{-1}$[63] ☑ Defect tolerant ☑ Feasible ambipolar doping ☒ Existing ion migration	☑ High PCE: up to 22.7%[16] ☑ High V_{oc}, J_{sc}, and fill factor ☑ Large cell area[64–66] ☑ Good reproducibility ☒ Existing photocurrent hysteresis
	Double perovskites ($A_2MM'X_6$)	☑ Lead free ☑ Good stability ☑ Diverse chemical compositions ☒ Poor film quality	☑ Having members with direct bandgaps ☒ Indirect or dipole-forbidden optical gaps ☒ Relatively large gap values ☒ Poor reported carrier transport	☒ Low PCE: up to ≈2.5%[48]
	Ordered-vacancy double perovskites (A_2MX_6)	☑ Lead free ☑ Thermodynamic stability	☑ Reasonable bandgap ☒ Existence of deep mid-gap defect states	☒ Low J_{sc} ☒ Poor PCE: up to ≈1%[55]
	2D perovskites ($A'_2A_{n-1}M_nX_{3n+1}$)	☑ Improved material stability ☑ Low-cost synthesis ☒ Containing toxic lead	☑ Variable bandgaps with layer thickness ☑ High-threshold light absorption ☒ Bad carrier transport perpendicular to the layers	☑ Relatively high PCE: up to 13.7%[45] ☑ High V_{oc}, J_{sc}, and fill factor ☑ Large cell area (up to 2.32 cm^2)[50] ☑ Negligible photocurrent hysteresis ☑ Robust reproducibility
	Perovskite-like materials ($A_3M_2X_9$)	☑ Lead free ☑ Good material stability	☑ Reasonable quasi-direct bandgaps for the layered phases ☒ Large indirect bandgaps for the dimer phases	☒ Low J_{sc} ☒ Low PCE: up to 1.64%[31]
Nonhalide perovskites	Chalcogenide perovskites (ABS/Se_3, $A_3B_2S_7$)	☑ Lead free ☑ Thermodynamic stability ☒ Poor film quality	☑ Suitable bandgaps ☑ Reasonably high threshold light absorption ☒ Poor carrier transport	☒ No reported devices
	Ferroelectric oxide perovskites (ABO_3, $A_2BB'O_6$)	☑ Strong material stability	☑ Polarization field favorable for charge separation ☒ Oversized bandgap ☒ Low carrier conductivity	☑ Reported PCE: up to 8.1%[56] ☑ V_{oc} beyond the bandgap ☑ Potential large cell area ☒ Poor reproducibility

contributes to its high PV performance. On one hand, the large dielectric constant weakens the Coulomb interactions between electrons and holes, leading to a low exciton binding energy down to 2 meV,[59–61] which is beneficial for the electron and hole separation process. On the other hand, the large dielectric constant provides effective screening of the charged defects and impurities, thereby reducing the carrier scattering and trapping and consequently increasing the carrier lifetime.[83] Based on first-principles defect calculations, Yin et al.[67] found that the transition levels of most intrinsic defects for cubic $MAPbI_3$ are shallow, while defects that create deep levels have high formation energies (as shown in Figure 2e) and thus have low concentration. This defect tolerant feature is qualitatively supported by other calculations.[84,85] A low concentration of carrier traps and nonradiative recombination centers are responsible for the superlong photogenerated carrier diffusion lengths (>1 μm)[62] and prolonged carrier lifetimes.[86] Meanwhile, $MAPbI_3$ exhibits flexible carrier conduction from good p-type, intrinsic, to good n-type depending on the growth conditions.[67]

Therefore, hybrid organic–inorganic perovskites meet almost all the requirements for best-performance PV applications (e.g., items 1–8 in Table 1). The certified PCE of thin-film solar cells based on $MAPbI_3$-based perovskites

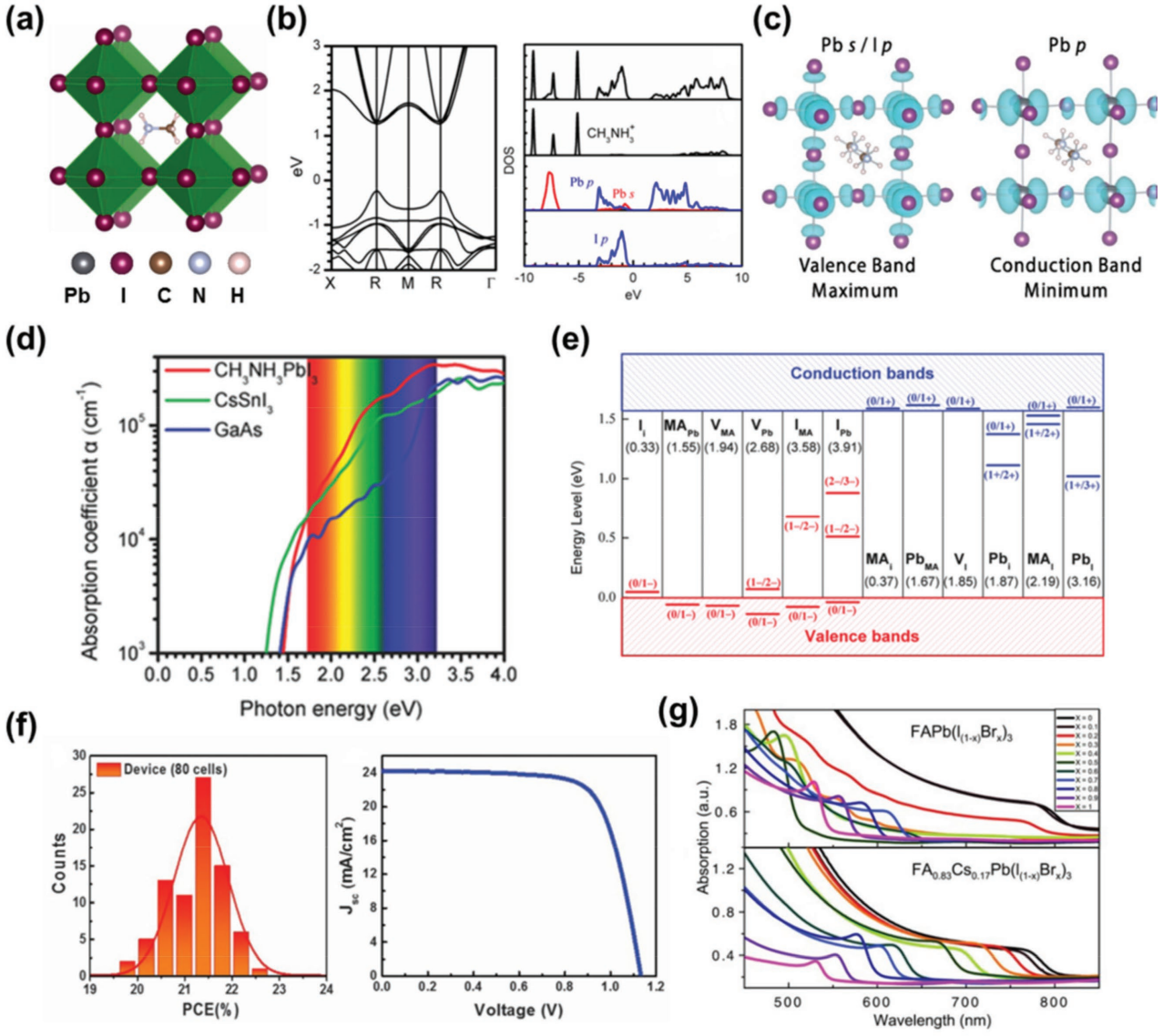

Figure 2. a) Crystal structure of $MAPbX_3$ perovskites (MA = methylammonium; X = I, Br, or Cl). b) The calculated band structure and DOS of $MAPbX_3$ using the DFT-PBE (Perdew-Burke-Ernzerhof functional) method. Adapted with permission.[67] Copyright 2014, AIP Publishing. c) Isosurface plots of the self-consistent electron densities of the upper valence and lower conduction bands of $MAPbI_3$. Adapted with permission.[68] Copyright 2013, AIP Publishing. d) Calculated optical absorptions of $MAPbI_3$, $CsSnI_3$, and GaAs. Adapted with permission.[69] Copyright 2014, Wiley-VCH. e) Calculated transition energy levels of point defects in $MAPbI_3$. The formation energies of neutral defects are shown in parenthesis. The red and blue lines represent the acceptors and donors, respectively. Adapted with permission.[69] Copyright 2014, Wiley-VCH. f) Histogram of the average power conversion efficiency determined for 80 perovskite solar cells (left) and *J*–*V* curve for a large-area cell (1 cm^2) plotted as the average of the reverse- and forward-scan modes and the corresponding PV parameters (right). Adapted with permission.[64] Copyright 2017, Science. g) UV–vis absorption spectra of $FAPb(I_{1-x}Br_x)_3$ and $FA_{0.83}Cs_{0.17}Pb(I_{1-x}Br_x)_3$ thin films (FA = formamidinium). Adapted with permission.[70] Copyright 2016, Science.

has rapidly increased to 22.1% in small cells (as shown in Figure 2f)[64] and 19.7% in 1 cm^2 cells[64] with reasonable device reproducibility. The lab efficiency is already on par with other conventional thin-film solar cells (22.1% for CdTe and 22.6% for CIGS[16]). It took merely eight years for perovskite materials to achieve this high PCE, while all other solar materials have been developed for decades to reach similar PCEs.

Despite the demonstrated high PCE, two key challenges (i.e., items 9–10 in Table 1) currently impede the large-scale application of halide perovskite PV technology. First, the devices show poor long-term stability under high temperature and outdoor illumination, as well as in the presence of moisture or oxygen, which is ascribed to intrinsic thermodynamic instability. Second, the use of toxic Pb is a serious environmental concern. There is thus strong desire to replace Pb with other environment-friendly elements while maintaining a similar high PV performance.[11,87–89] Other technical issues, such as reducing the bandgap to the optimal value of 1.34 eV to approach the Shockley–Queisser limit, are

also expected to be addressed simultaneously while solving the aforementioned two key challenges.

2.2. Elemental Substitution/Composition Engineering in Single Perovskites

In efforts to improve efficiency and stability of solar cells, chemical composition engineering through A-site, M-site, and X-site substitution or alloying has been demonstrated to be an effective strategy.[15,17–22,24,37,90–94]

Mixing halogen elements at X sites have several beneficial effects, for example, improving the material stability, enhancing carrier transport, and tuning the bandgap. For instance, Lee et al.[21] found that $MAPb(I_{1-x}Cl_x)_3$ showed remarkable stability during processing in air compared to $MAPbI_3$. Noh et al.[22] demonstrated that mixing 20–29% Br into $MAPbI_3$ greatly improved the solar-cell stability. The observed experimental phenomena are in accordance with theoretical predictions by first-principles calculations.[95] Longer electron and hole carrier diffusion lengths than those in $MAPbI_3$ were observed in $MAPb(I_{1-x}Cl_x)_3$ by transient absorption and photoluminescence (PL)-quenching measurements.[62,86,93] $MAPb(I_{1-x}Br_x)_3$ and $MAPb(Br_{1-x}Cl_x)_3$ were also demonstrated to possess improved carrier mobility and reduced carrier recombination rates.[91,94] For bandgap tuning, continuously tuning gap values has been achieved in $MAPb(Br_{1-x}Cl_x)_3$.[91] Solar cells based on $MAPbBr_3$ and $MAPb(Br_{1-x}Cl_x)_3$ have achieved open-circuit voltages (V_{oc}) up to 1.3 and 1.5 eV, respectively.[91,96] Halide perovskites with increased bandgaps have been used as the active layers of top cells in multijunction solar cells to enhance the PCE.[91,94,97] In addition to halogen anions, pseudo-halogens with similar electronegativities and chemical properties (e.g., SCN^- and BF_4^-) have also been considered. Since perovskites with SCN^- and BF_4^- possess bandgaps higher than the upper limit of the visible spectrum,[97] they are not suitable materials for single-junction solar cells. Nevertheless, alloying them with the AMX_3 halide perovskites offer a possible degree of freedom to improve the material stability and modify optoelectronic properties. As examples, Jiang et al.[98] demonstrated that solar cells based on $MAPb(SCN)_2I$ showed drastically improved moisture tolerance and thermodynamic stability while achieving a PCE of 8.3%. Nagane et al.[99] observed that a small fraction of BF_4^- incorporated into $MAPbI_3$ resulted in a slightly blueshifted absorption onset at 760 nm but gave a one order of magnitude enhancement in the low frequency electrical conductivity and improved photoresponse under AM 1.5 illumination.

Replacement of organic MA cations with larger FA cations in $MAPbI_3$ tends to form a trigonal structure containing distorted $[PbI_6]$ octahedra. The bandgap of the black $FAPbI_3$ phase was found to be 1.48 eV,[100] smaller than that of $MAPbI_3$ (1.5 eV)[43,58] and closer to the optimal gap value of 1.34 eV. This feature could potentially provide a higher PCE.[100] However, the black trigonal $FAPbI_3$ phase has poor stability and is easily transformed into a yellow hexagonal perovskite-like phase with a wide bandgap of 2.48 eV.[101] This issue has been resolved by mixing a small amount of inorganic cations, such as Cs, into the FA sites, which significantly improves stability of the perovskite films.[17,24,70,102] The underlying mechanism has been attributed to the tolerance factor, t, which is effectively tuned in $FA_{1-x}Cs_xPbI_3$.[17] According to McMeekin et al.,[70] the absorption onsets of $FA_{0.83}Cs_{0.17}Pb(I_{1-x}Br_x)_3$ and $FAPb(I_{1-x}Br_x)_3$ can be continuously tuned through the entire compositional range (as shown in Figure 2g). It was observed that the absorption is stronger in the case of co-alloying A-site cations and X-site anions than the case of X-site alloying only. Thus, tuning the tolerance factor through co-alloying could be a promising strategy to be further explored to enhance the stability and tune the optoelectronic properties.

Turning to the compositional engineering of M sites, the straightforward strategy for Pb elimination is to replace Pb using other divalent cations. The same group-IVA cations Sn^{2+} and Ge^{2+} have been considered. By partially replacing Pb^{2+} with Sn^{2+}, Li et al.[25] obtained high-quality $MASn_{0.5}Pb_{0.5}I_3$ films with high reproducibility and achieved an impressive PCE of 13.6%. The bandgap of $MASn_{0.5}Pb_{0.5}I_3$ perovskite is 1.18 eV, lower than that of $MAPbI_3$. Lead-free halide perovskites have also been experimentally synthesized and reported. Solar cells made with $MASnI_3$ and $FASnI_3$ have been reported with PCEs of approximately 5.73 and 6.22%,[103,104] respectively. The absorption onsets of $MASnI_3$ and $FASnI_3$ are approximately 950 and 900 nm, corresponding to bandgaps of 1.3 and 1.37 eV, respectively, which are significantly redshifted compared with those of $MAPbI_3$ and $FAPbI_3$. However, the devices suffered from rapid degradation when exposed to air,[105–112] caused by the instability of the Sn^{2+} cations (prone to oxidation to Sn^{4+}). Ge-based halide perovskite $MAGeI_3$ has been synthesized, which shows substantial distortion from the perfect perovskite framework and a gap value of 1.9 eV.[108] This material is not an ideal solar absorber because of the similar high oxidation tendency of Ge^{2+} and emergence of deep defect states.[108–110] Using theoretical studies, Yang et al.[97] performed PV-functionality-directed material screening of hundreds of AMX_3 perovskites and identified a series of new Sn/Ge-based perovskites with promising PV performance. The mixed Sn and Ge halide perovskites have also been proposed as potential Pb-free solar perovskites.[111] These predictions still await future experimental verification. Nevertheless, the instability associated with the tendency of oxidation of Sn^{2+}/Ge^{2+} to Sn^{4+}/Ge^{4+} is still an inevitable challenging issue to overcome. Replacing Pb^{2+} with other divalent cations beyond the IVA group (such as Mg, Sr, or Ba)[105–107] has also been explored, but unfortunately the resulting materials show oversized bandgaps unsuitable for solar applications.

2.3. Heterovalent-Substitution-Derived Double Perovskites

In addition to the isovalent substitution of Pb with alternative M^{2+} cations in single perovskites, heterovalent substitution has been demonstrated to be an efficient strategy to design new halide perovskites. The idea originates from the so-called "cation transmutation" strategy in traditional tetrahedral

semiconductors: by transmuting two Zn^{2+} ions in ZnSe into one Cu^+ and one Ga^{3+}, that is, $2Zn^{2+} \rightarrow Cu^+ + Ga^{3+}$, $CuGaSe_2$ in the CIGS family of solar absorbers is obtained. By adapting this idea in halide perovskites, as illustrated in **Figure 3**a, two Pb^{2+} cations can be replaced by a cation pair $[M^+ + M'^{3+}]$ while maintaining the total charge states of the cation sites. The resulting double perovskites, $A_2MM'X_6$ (in space group $Fm\bar{3}m$), features an ordered rock-salt-like arrangement of corner-shared MX_6 and $M'X_6$ units. Double halide perovskites are attractive by providing more freedom in selecting the cation elements.

By following this design principle and taking Bi^{3+}/Sb^{3+} (isoelectronic to Pb^{2+}) as M'^{3+} cations, a series of Pb-free $A_2MM'X_6$ double perovskites have been theoretically and experimentally designed.[26,27,115–117] In the theoretical work by Zhao et al.,[113] PV-functionality-directed materials screening involving 64 $A_2MM'X_6$ candidates was carried out, where A = Cs^+, M = group IA (Na^+, K^+, or Rb^+), group IB (Cu^+, Ag^+, or Au^+), or group IIIA (In^+ or Tl^+), M′ = Bi^{3+} or Sb^{3+}, and X = F^-, Cl^-, Br^-, or I^-. The electronic band structures of these double perovskites can be classified into three categories according to the M^+ cation, as indicated in Figure 3b (upper panel): (1) type-I with M^+ being group-IA elements (Na^+, K^+, or Rb^+) that have empty s and d valence orbitals, (2) type-II with M^+ being group-IB elements (Cu^+, Ag^+, or Au^+) that have empty s but full d valence orbitals, and (3) type-III with M^+ being group-IIIA elements (In^+ or Tl^+) that have full s valence orbitals. Figure 3b (lower panel) shows that while the bandgaps show general translational shifting trends upon changing X- anions, the variation of bandgaps can be increased or decreased depending on the choice of M^+ cations. Among these types of $A_2MM'X_6$ double perovskites, the type-I group generally has quite large bandgaps above 3.0 eV,[113] unsuitable for solar applications.

For the type-III Bi^{3+}/Sb^{3+}-based double perovskites represented by $Cs_2InBiCl_6$, the electronic structure resembles that of $MAPbI_3$, as shown in Figure 3b.[113] The bandgap is direct at the Γ point. The VBM consists mainly of antibonding states of In 5s and Cl 3p orbitals, and the CBM is composed

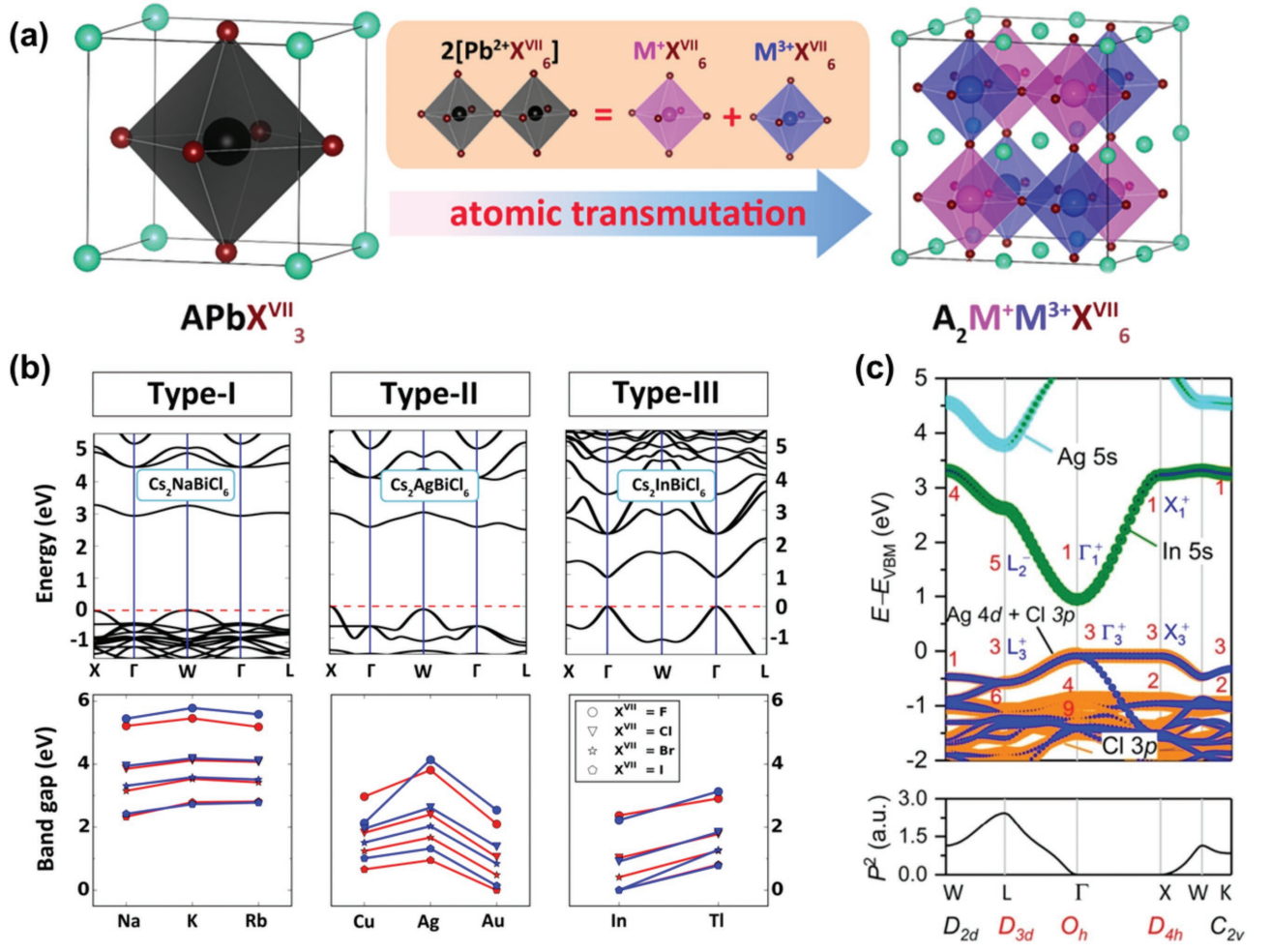

Figure 3. a) Illustration of the cation transmutation strategy (converting 2 Pb^{2+} to a pair of $[M^+ + M'^{3+}]$) to design Pb-free halide double perovskites. b) Calculated band structures of three categories of $A_2M^+M'^{3+}X_6$ (M^{3+} = Bi/Sb) materials (upper panels) and variation of bandgaps with the M^+ element. The Bi- and Sb-based materials are shown in blue and red, respectively. a,b) Adapted with permission.[113] Copyright 2017, American Chemical Society. c) Calculated band structure and optical transition matrix elements for $Cs_2AgInCl_6$ using the DFT-PBE method. Reproduced with permission.[114] Copyright 2017, American Chemical Society.

mainly of antibonding states of Bi 6p and Cl 3p orbitals. Such an electronic structure is expected to give low and balanced carrier effective masses, strong optical absorption, defect tolerant feature, etc., similar to $MAPbI_3$. These are in favor of high PV performance. Thus far, the $A_2In^+(Bi^{3+}/Sb^{3+})X_6$ compounds have not been experimentally synthesized, likely owing to the strong tendency of In^+ being oxidized into In^{3+}. Recently, Volonakis et al.[118] proposed that the use of large-size organic molecules might enable stabilization of $A_2In^+(Bi^{3+}/Sb^{3+})X_6$ compounds, which awaits future experimental verification.

For type-II Bi^{3+}/Sb^{3+}-based double perovskites, $Cs_2AgBiBr_6$ (E_g = 1.95 eV),[26] $Cs_2AgBiCl_6$ (E_g = 2.77 eV),[116] and $Cs_2AgSbCl_6$ (E_g = 2.54 eV),[119] have been experimentally synthesized. For these double halide perovskites, all exhibit enhanced stability when exposed to ambient air and light. The bandgap of $Cs_2AgBiCl_6$ is, however, too large for solar-cell applications. $Cs_2AgBiBr_6$ shows the characteristics of an indirect-gap semiconductor with a slow-rising absorption followed by a sharp increase.[26] By using the Tauc plot of the absorption spectrum, the indirect bandgap of $Cs_2AgBiBr_6$ was evaluated to be 1.95 eV, and the direct bandgap was 2.07 eV. The result is in accordance with first-principles calculations.[113] According to a recent report by Du et al.,[120] the large indirect bandgap of $Cs_2AgBiBr_6$ can be reduced by ≈0.41 eV through introducing 37.5% Sb^{3+}, and thus, the $Cs_2Ag(Bi_{0.675}Sb_{0.375})Br_6$ mixture shows a lower bandgap of 1.86 eV. Moreover, Slavney et al.[121] demonstrated that $Cs_2AgBiBr_6$ can afford a reduction of ≈0.5 eV in bandgap via dilute Tl alloying while accompanying long-lived carriers with a microsecond lifetime.

Recently, Greul et al.[67] demonstrated for the first time the fabrication of $Cs_2AgBiBr_6$ films and incorporated them into working devices. The solar cell made with the $Cs_2AgBiBr_6$ film exhibited a promising PCE close to 2.5% and a V_{oc} exceeding 1 V, which is currently the highest V_{oc} reported for Bi-based halide perovskites. In addition, the $Cs_2AgBiBr_6$-based device possessed high stability under constant illumination under ambient conditions, higher than that of reported $MAPbI_3$-based devices showing a significant drop of the short-circuit current (J_{sc}) within the first 2 h.[40] The $(MA)_2AgBiBr_6$ compound derived from $Cs_2AgBiBr_6$, replacing Cs with the organic molecule MA, has also been experimentally synthesized by Wei et al., showing an indirect bandgap of 2.02 eV.[122] Recently, Cheng et al.[123] synthesized $(MA)_2AgBiI_6$ with an indirect bandgap of 1.96 eV. As it is the first iodide double perovskite reported, further efforts might be needed to verify its existence and characterize its properties.

Apart from the above double perovskites involving Bi^{3+}/Sb^{3+}, by transmuting two Pb^{2+} to a $[M^+ + M'^{3+}]$ pair, such as [Cu + Ga], [Ag + In], or combinations thereof, Zhao et al.[124] proposed based on first-principles calculations a new group of CuIn-based halide perovskite (CIHP). The new proposed compounds showed direct bandgap, with the best-of-class members (for PV applications) of $Cs_2[AgIn]Cl_6$, $Cs_2[AgIn]Br_6$, $Rb_2[AgIn]Cl_6$, $Rb_2[AgIn]Br_6$, $Rb_2[CuIn]Cl_6$, and $Rb_2[CuIn]Br_6$. Independently, the CIHP compound $Cs_2[AgIn]Cl_6$, was synthesized in a joint experiment-theoretical study by Volonakis et al.[125] The calculated band structure of $Cs_2[AgIn]Cl_6$ with a direct bandgap at the Γ point is shown in Figure 3c (upper panel). The VBM is mainly derived from Ag 4d and Cl 3p orbitals, and the CBM is derived from delocalized In 5s states, which lead to a dispersive bottom conduction band. Although possessing a direct bandgap, $Cs_2[AgIn]Cl_6$ showed a slow-rising absorption near the threshold,[124] in agreement with experimental observation.[125] The underlying mechanism can be attributed to the inversion-symmetry induced parity-forbidden transition at the band edge at the Γ point.[114] The parity of the conduction band edge changes when the k point moves away from the Γ point, while the parity of the valence band edge does not. Therefore, the calculated dipole transition matrix element increases as the k point changes from the Γ to L point, as shown in Figure 3c (bottom panel). This explains the gradually rising absorption curve away from the threshold. Cu^+-containing double perovskites have not been experimentally reported thus far. In a recent work by Xiao et al.,[126] the authors argued that the synthesis of Cu(I)-based halide perovskites may instead lead to products containing $[CuX_4]$ tetrahedra, owing to the much higher energy levels of Cu 3d orbitals than those of Ag 4d orbital.

2.4. Ordered-Vacancy Double Perovskites

In addition to $A_2MM'X_6$ double perovskites, ordered-vacancy double perovskites with the general formula A_2MX_6 are a family of perovskites composed of a face-centered lattice of nearly isolated $[MX_6]$ units with A-site cations occupying the cuboctahedral voids, as shown in **Figure 4**a. As a typical example, Cs_2SnI_6 has been reported exhibiting some promising properties, such as a suitable bandgap and air stability for PV applications. The calculated band structure and DOS of Cs_2SnI_6 with the HSE hybrid functional are shown in Figure 4b.[127] The band structure of Cs_2SnI_6 exhibits a direct bandgap of 1.26 eV at the Γ point,[127] which is consistent with the experimental value obtained from the absorption spectrum.[129,131] Although Cs_2SnI_6 is structurally similar to $CsSnI_3$ by removing half of the Sn atoms from alternating sites, it has a distinct electronic structure, which is schematically illuminated in Figure 4c.[128] In $CsSnI_3$, the VBM consists of antibonding states between the Sn 5s and I 5p orbitals, while in Cs_2SnI_6, the antibonding states are between I 5p orbitals. The CBM in $CsSnI_3$ is composed of nonbonding states of Sn 5p orbitals, while in Cs_2SnI_6, the CBM is composed of antibonding states of Sn 5s and I 5p orbitals.

The solid-state dye-sensitized solar cells using Cs_2SnI_6 as a hole transporter were reported with PCEs of ≈4.7 and near 8% with photon confinement using a more efficient mixture of porphyrin dyes.[129] In comparison with Sn^{2+} perovskites, the stability is improved significantly with a lifetime at least an order of magnitude longer, as shown in Figure 4e. Figure 4f shows the calculated band structure and DOS of Cs_2PdBr_6 with the HSE hybrid functional, where it can be seen that Cs_2PdBr_6 has an indirect bandgap with the VBM located at the Γ point and CBM located at the X point.[130] According to the calculations, Cs_2PdBr_6 should behave as an n-type semiconductor with a higher electron mobility than hole mobility owing to the presence of a heavy hole band at the VBM. The calculated bandgap of 1.56 eV from DFT-HSE is in agreement with the observed

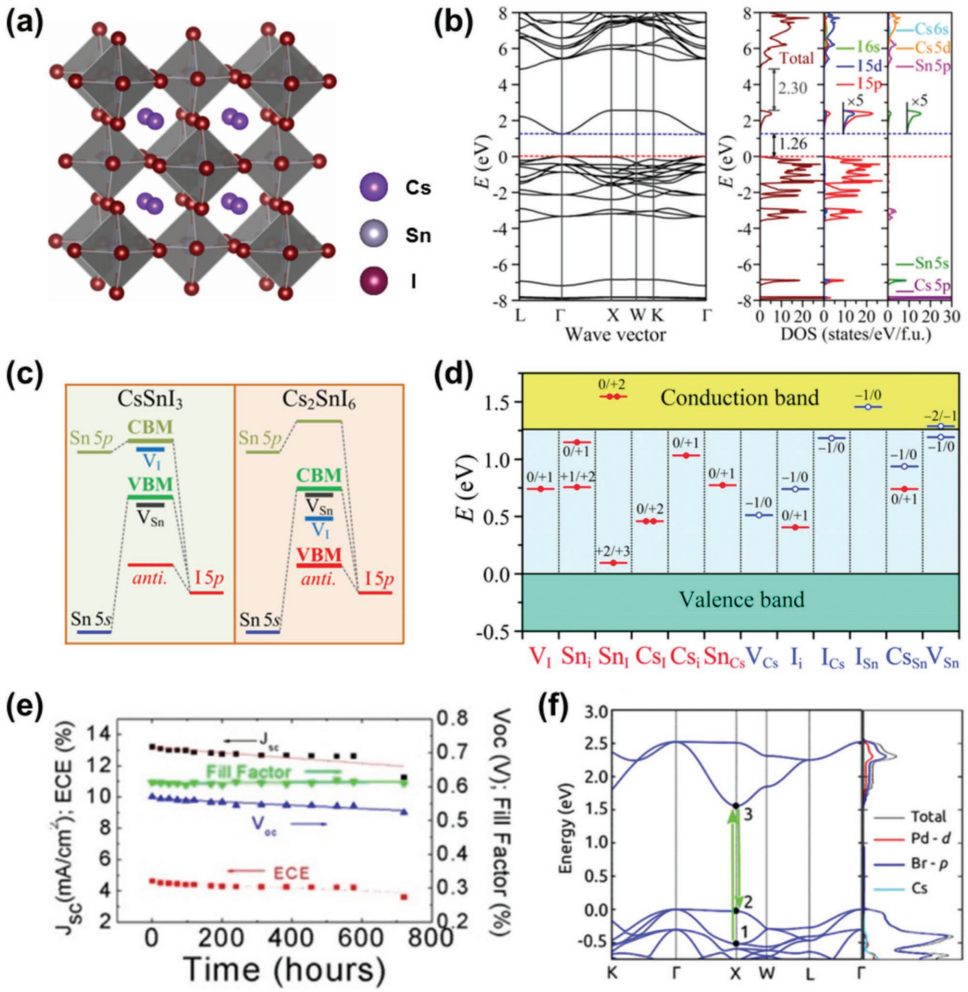

Figure 4. a) Crystal structure of Cs_2SnI_6. b) Calculated band structure and total and projected DOS of Cs_2SnI_6 with the HSE functional. b) Reproduced with permission.[127] Copyright 2015, The Chemical Society of Japan. c) Simplified energy diagrams depicting the formation of VBM/CBM and donor-/acceptor-like defects in $CsSnI_3$ (left) and Cs_2SnI_6 (right). d) Calculated transition energy levels for intrinsic defects in Cs_2SnI_6. Donor and acceptor defect levels are denoted by the red and blue lines, respectively. The solid and open circles at the transition levels show the number of electrons and holes that can be released during the transition of the defect charge state. c,d) Reproduced with permission.[128] Copyright 2015, Royal Society of Chemistry. e) Long-term measurement of a solid-state dye-sensitized solar cell based on Cs_2SnI_6 taken at regular intervals as a function of time. Reproduced with permission.[129] Copyright 2017, American Chemical Society. f) Electronic band structure and projected DOS of Cs_2PdBr_6. The black dots mark the second highest (1) and highest (2) occupied state and the lowest unoccupied state (3) at the X point. Reproduced with permission.[130] Copyright 2017, American Chemical Society.

bandgap from PL measurements. More importantly, Cs_2PdBr_6 is resistant to water, in contrast to the lead halide single perovskites. Among the family of ordered-vacancy double halide perovskites, Cs_2TeI_6 with a bandgap of 1.59 eV has also been experimentally synthesized.[130,132] With favorable bandgaps, the ordered-vacancy double halide perovskites (i.e., Cs_2MX_6, M = Sn, Te, or Pd; X = I or Br) could potentially be used as solar absorbers. Being low cost, stable, lead free, and environmentally benign also makes them attractive materials.

However, a caveat was reported in the recent work by Xiao et al.,[133] where the authors demonstrated that the so-called "electronic dimensionality" (the connectivity of the atomic orbitals that contribute to the lower conduction band and upper valence band) could better account for the PV properties of perovskite absorbers than structural dimensionality, with high electronic dimensionality providing the opportunity for (though not guaranteeing) high PV performance. Reduced electronic dimensionality will induce increases of the bandgap and effective mass. In this regard, the A_2MX_6 compounds exhibit low structural dimensionality and electronic dimensionality and therefore might be less promising as solar absorbers.

2.5. 2D Halide Perovskites

2D halide perovskites have been recently realized experimentally and have demonstrated attractive properties for PV applications. Layered perovskites can be structurally derived from 3D AMX_3 perovskites by slicing along specific crystallographic planes. The crystal structures of 2D layered perovskites with a

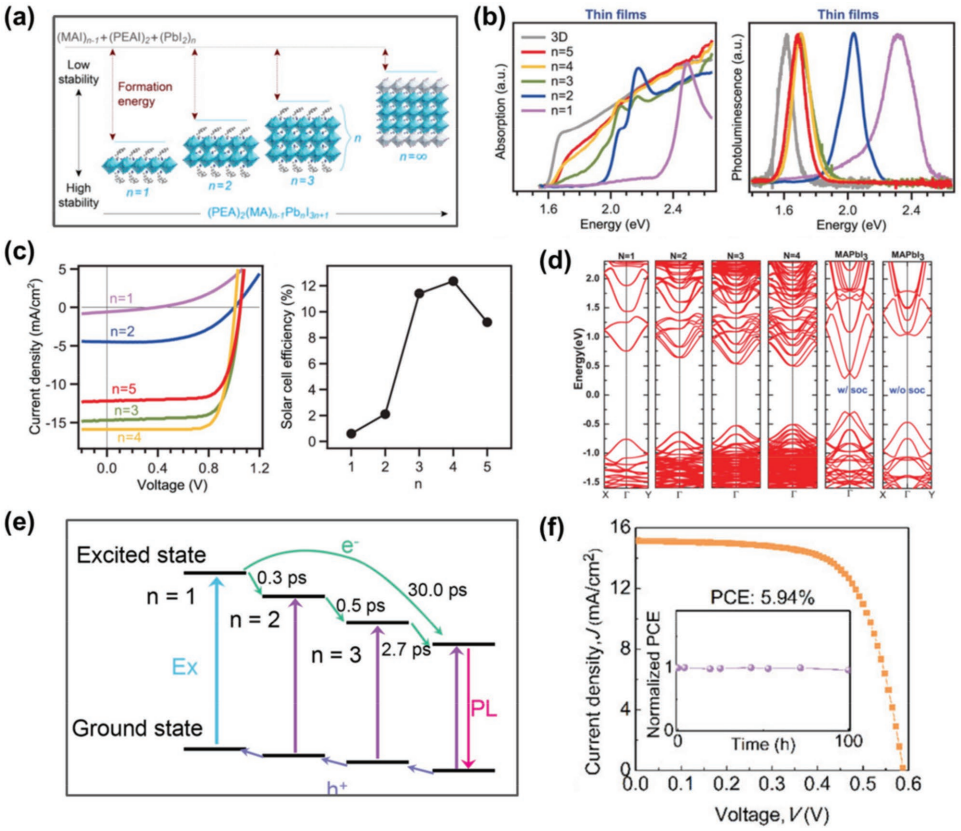

Figure 5. Unit-cell structures of $(C_8H_9NH_3)_2(CH_3NH_3)_{n-1}Pb_nI_{3n+1}$ perovskites with different n values, showing the evolution of dimensionality from 2D (n = 1) to 3D (n = ∞). Adapted with permission.[29] Copyright 2017, American Chemical Society. b) Experimental absorptions of $(BA)_2MA_{n-1}Pb_nI_{3n+1}$ thin films at various n values. c) Current-density–voltage (J–V) curves measured under AM.1.5 illumination of $(BA)_2MA_{n-1}Pb_nI_{3n+1}$ thin-film devices and the corresponding PCEs as a function of the 2D perovskite n value. Reproduced with permission.[134] Copyright 2017, Science. d) Calculated band structures of $PEA_2MA_{n-1}Pb_nI_{3n+1}$ with n = 1–4 by PBE+SOC compared with that of $MAPbI_3$ with and without SOC. Reproduced with permission.[135] Copyright 2017, American Chemical Society. e) Schematic of the carrier transfer in the n = 3 quasi-2D perovskite film. Reproduced with permission.[136] Copyright 2017, American Chemical Society. f) Current-density–voltage (J–V) characteristics of the highest-performance device based on highly oriented $(PEA)_2(FA)_8Sn_9I_{28}$. The inset indicates the normalized PCE of the device stored in a glove box for over 100 h. Reproduced with permission.[137] Copyright 2017, American Chemical Society.

general formula of $A'_2A_{n-1}M_nX_{3n+1}$ are illustrated in **Figure 5**a (where A′ = long-chain organic molecules such as $C_4H_9NH_3^+$ (abbreviated as BA) or $C_6H_5(CH_2)_2NH_3^+$ (abbreviated as PEA), M = divalent metal elements, and X = halides).[28,29] The anionic 2D perovskite layers are passivated by the long-chain organic cations forming neutral slabs, which are stacked together by weak van der Waals forces. n = 1 corresponds to monolayer 2D perovskite layers, while n = ∞ corresponds to the 3D bulk perovskite phase. DFT-based calculations indicate that the thermodynamic stability is enhanced with a reduction of n compared with the 3D counterpart, which is in agreement with experimental observations.[29,44]

Figure 5b shows the optical absorption spectra and PL spectra, which exhibit a gradual redshift with the octahedral layers increasing from one layer to infinite layers.[134] Bandgaps of 2.57 and 1.52 eV for single-layer PEA_2PbI_4 and the 3D $MAPbI_3$ bulk phase have been reported in previous works.[58,138] Figure 5c shows the experimental current-density–voltage (J–V) curves and PCEs of solar cells using 2D $(BA)_2(MA)_{n-1}Pb_nI_{3n+1}$ perovskites as absorbing layers measured under AM 1.5 illumination. The efficiencies of the unencapsulated devices using thin films of 2D $(BA)_2(MA)_3Pb_4I_{13}$ exceeded 12% with no hystereses under constant AM 1.5 illumination.[28,134] Zhang et al.[45] demonstrated that doping cesium (Cs) into 2D $(BA)_2(MA)_3Pb_4I_{13}$ perovskite helped increase the grain size, improve the surface quality, reduce the trap-state density, and enhance the charge-carrier mobility and charge-transfer kinetics, leading to a higher PCE of 13.7% and negligible hysteresis. The planar solar cells using $PEA_2MA_{n-1}Pb_nI_{3n+1}$ with n = 60 as an absorbing layer have a certified PCE of 15.3%.[29] More importantly, the long-term stability and cell performance of multilayer halide perovskites are significantly improved in comparison to their 3D counterparts, as demonstrated in duration measurements under ambient conditions.[28,29,44,139–142]

Figure 5d shows the calculated band structures of $PEA_2MA_{n-1}Pb_nI_{3n+1}$ (n = 1–4) by the DFT-based calculations including SOC.[135] The bandgap is located at the Γ point. When n increases, the VBM increases, while the CBM decreases, leading to a decrease of the bandgap. It should be noted that

the presented band alignment may not be correct, as the DFT energy levels at different n do not have a unified reference. This deserves further study. The effective masses of $PEA_2MA_{n-1}Pb_nI_{3n+1}$ only slightly vary as n increases. It is suggested that the mobilities of photogenerated carriers in the layered perovskites are still large enough for PV applications. Additionally, a giant SOC effect can be seen from the band structures, which split both the valence band and conduction band. The band splitting may be related to the Rashba effect under the condition of broken symmetry, which has been reported to enhance the carrier lifetime in $MAPbI_3$.[75]

In a planar solar cell, carrier transport between the different layers is driven by electrostatic potential differences near the interfaces, which facilitate the injection of photogenerated carriers into the carrier-transport layers before recombination. A unique spontaneous charge separation property in multilayered 2D perovskite films was reported.[136,143] Figure 5e shows the schematic of carrier transfer in a multiple-phase perovskite film.[135] Driven by the band alignment, photoinduced electrons are transferred downstream from small-n to large-n perovskite phases, while the holes are transferred upstream from large-n to small-n perovskite phases acting as a p–n junction-like device, ensuring carrier separation. The approach of mixing multiple perovskite phases by tailoring the composition of 2D layered perovskites could enable more efficient solar cells and more versatile applications in optoelectronic devices.

Low-dimensional Sn perovskites have been explored as solar-cell absorbers due to their low toxicity and markedly enhanced air stability in comparison with their 3D counterparts.[137,144] It has been reported that the PCE of a solar cell based on highly oriented low-dimensional Sn perovskite film reached 5.94% without the requirement of further device structure engineering, as shown in Figure 5f. More importantly, the unencapsulated solar cells showed no appreciable decay in efficiency over 100 h. This progress made by Liao et al.[137] raises the prospects of pure Sn perovskites for solar-cell applications.

2.6. Perovskite-Like Materials

Trivalent-metal halide compounds with the general formula of $A_3M_2X_9$, where A = Cs^+ or MA^+, M = Sb^{3+}or Bi^{3+}, X = Cl^-, Br^-, or I^-, have attracted significant attention because they have better stability and lower toxicity than Pb-based halide perovskites. There are two typical variations of $A_3M_2X_9$ compounds reported experimentally: a phase composed of 2D corrugated layers with partially corner-sharing MX_6 octahedra, referred to as the layer phase, with a space group of $P\bar{3}m1$, and a hexagonal phase consisting of 0D bioctahedral face-sharing $(M_2X_9)_3$ clusters, referred to as the dimer phase, with a space group of $P6_3/mmc$.

Taking $Cs_3Sb_2I_9$ as an example, the left panel of **Figure 6**a shows the crystalline structures of the two phases. The layer phase is a one-third M-deficient derivative of the prototype 3D perovskite structure, where two M-atom layers alternately stack along the ⟨111⟩ direction of the cubic perovskite structure. The right panel of Figure 6a shows the band structures of the two phases using the HSE functional. The calculated bandgaps are 2.06 and 2.40 eV for the layer and dimer phases, respectively, which are in good agreement with the experimental values of 2.05 and 2.44 eV, respectively.[30] The large bandgap of the dimer phase may be related to the reduced structural dimensionality. Bi-based materials, such as $Cs_3Bi_2I_9$ and $MA_3Bi_2I_9$, only crystallize in a hexagonal phase (dimer phase) with reported bandgaps of 2.14 and 2.1 eV, respectively.[46,145] Park et al.[46] reported solar cells based on $Cs_3Bi_2I_9$ and $MA_3Bi_2I_9$ with PCEs of 1.09 and 0.12%, respectively. Zhang et al.[31] reported a higher efficiency of 1.64% based on $MA_3Bi_2I_9$ with improved processing, such as high-vacuum BiI_3 deposition and low-vacuum homogeneous transformation of BiI_3 to $MA_3Bi_2I_9$, which yield highly compact and pinhole-free films. While the PCE is still not competitive, the progress on this class of Pb-free materials has been impressive and has attracted intensive research on their material properties.

Pal et al.[146] revealed that the presence of deep-level defects, which act as recombination centers, is the major issue for the performance of Bi-based perovskite-like materials. The large bandgaps are an apparent issue that must be engineered. As mentioned above, layer-phase $Cs_3Sb_2I_9$ exhibits a reduced bandgap and redshifted absorption edge compared to the dimer phase. Figure 6b shows optical absorption of the layer phase of $Cs_3Sb_2I_9$.[30] By assuming a direct bandgap, the Tauc plot yields a gap of 2.05 eV, which is consistent with the orange color of the $Cs_3Sb_2I_9$ sample. The calculated absorption coefficients of the layer and dimer phases are compared with that of $MAPbI_3$ in Figure 6c. The absorption coefficient of the layer phase is as high as that of $MAPbI_3$. The high absorption coefficient of the layer phase can be understood by its electronic structure. The top valence band is comprised of I p and Sb s orbitals, and the bottom conduction band is mainly derived from Sb p orbitals. Thus, the composition of the frontier orbitals is similar to that of $MAPbI_3$, and therefore, a similarly high optical absorption coefficient is expected.

As shown in the band structure (right panel of Figure 6a), the layer phase has a quasi-direct bandgap with the CBM located at the Γ point and the VBM slightly deviated from the Γ point. The conduction and valence band edges are rather dispersive, indicating low effective masses of electron and hole carriers. The calculated effective masses with different theoretical methods[30] are lower than 1.0 m_0 along the [100] and [001] directions (though larger than that of $MAPbI_3$[77,78]). In this respect, the 2D layered polymorph of $Cs_3Sb_2I_9$ appears to be a promising stable solar absorber. Saparov et al.[30] investigated the defect properties of the layer phase of $Cs_3Sb_2I_9$. Their results suggest that all intrinsic defects create deep defect levels in the bandgap, which act as nonradiative recombination centers. The exceptions are V_{Cs} (Cs vacancies) and Cs_i (Cs interstitials), which are shallow acceptors and donors, respectively. Although $Cs_3Sb_2I_9$ is a perovskite derivative, these calculations indicate that the defect properties are quite different from that in $MAPbI_3$. Therefore, the defect properties of $Cs_3Sb_2I_9$ could be a main issue that requires careful control toward PV applications.[146]

In addition to the aforementioned materials with a stoichiometry of $A_3M_2X_9$, a low-toxicity Bi halide, $CsBi_3I_{10}$, with a bandgap of 1.77 eV, which is smaller than that of $Cs_3Bi_2I_9$, has been synthesized from a solution process. X-ray diffraction (XRD) measurement suggests that $CsBi_3I_{10}$ contains a layered structure similar to that of BiI_3, but the layers are partly broken

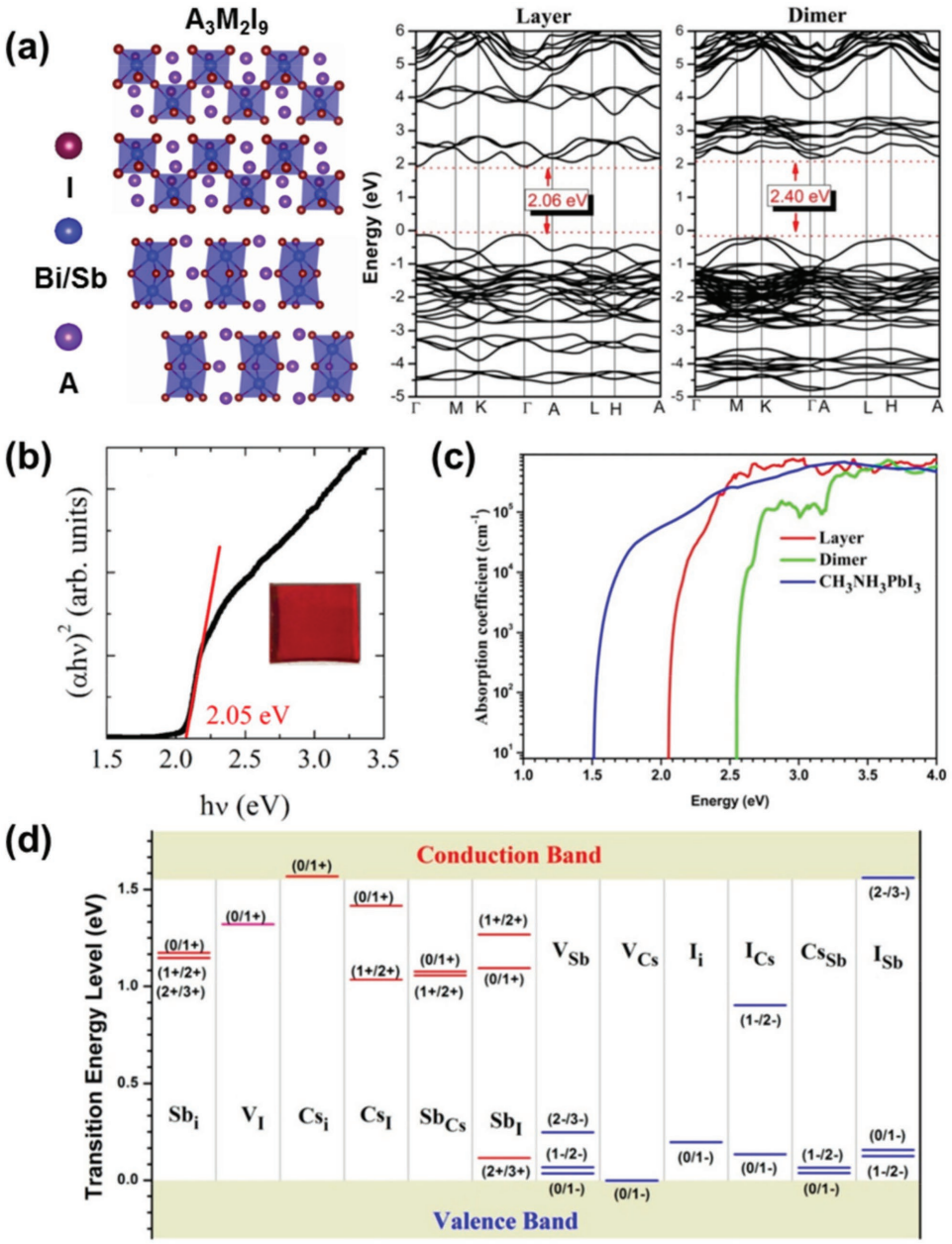

Figure 6. Crystal structures of $A_3M_2I_9$ with a 2D layer phase (upper panel) and 0D dimer phase (bottom panel) and calculated band structures of $Cs_3Sb_2I_9$ in the layer and dimer phases using the HSE functional. b) Optical absorption for determining the bandgap of layer-phase $Cs_3Sb_2I_9$ (inset shows a thin-film sample). c) Calculated absorption coefficients for $Cs_3Sb_2I_9$ in the layer and dimer phases compared to that of $MAPbI_3$. d) Calculated transition energy levels of the intrinsic donors (red lines) and acceptors (blue lines) in layer-phase $Cs_3Sb_2I_9$. Reproduced with permission.[30] Copyright 2017, American Chemical Society.

into a 0D structure with $Cs_3Bi_2I_9$ in between the layers.[147] Solar cells made from $CsBi_3I_{10}$ show considerably redshifted absorption spectra up to 700 nm compared to that of $Cs_3Bi_2I_9$ and exhibit good long-term stability under ambient conditions. The PCE has been reported to be low (≈0.4%).

Kim et al.[148] reported another Bi-based material, $AgBi_2I_7$. Thin films of $AgBi_2I_7$ exhibit a cubic structure (space group $Fd\bar{3}m$) with a bandgap of 1.87 eV. Solar cells based on $AgBi_2I_7$ achieved a PCE of 1.22% and maintained excellent stability over at least 10 d under ambient conditions. $AgBi_2I_7$ is closely related to $AgBiI_4$, which also has a cubic structure (space group $Fd\bar{3}m$)[149] but possesses an indirect bandgap of 1.63 eV, smaller than that of other Bi halides. According to the DFT study by Xiao et al.,[150] the $AgBi_2I_7$ structure is thermodynamically unstable and more likely to adopt the Ag-deficient $AgBiI_4$ structure. The structural relationship of the entire Ag-Bi-I system, including other reported compositions, such as Ag_2BiI_5 and Ag_3BiI_6,[151,152] requires further investigation.

3. Nonhalide Perovskites

3.1. Chalcogenide Perovskites

With the aim of solving the issues of toxicity and instability of lead halide perovskites, chalcogenide perovskites based on S and Se, as a new class of lead-free and stable alternatives, have been proposed and studied recently. With the ABX_3 stoichiometry, alkaline earth metals Ca, Sr, and Ba have been considered for the A site, transition metals Ti, Zr, and Hf have been considered for the B site, and X has been one of the chalcogens S or Se. A number of compounds, such as $CaZrS_3$, $SrTiS_3$, $SrZrS_3$, $BaTiS_3$, $BaZrS_3$, $CaHfS_3$, and $BaHfS_3$, have been experimentally synthesized. Three phases, including distorted perovskite, hexagonal, and needle-like phases, have been observed at room temperature, as shown in **Figure 7**a. Only $CaZrS_3$, $BaZrS_3$, $SrZrS_3$, $CaHfS_3$, and $BaHfS_3$ have been reported to exist in the distorted perovskite structure. The other compounds tend to crystallize in the hexagonal or needle phase.[155]

Through DFT-HSE calculations[153] on 18 compounds in the three phases, more than ten materials were found to absorb in the far-IR to visible spectral range (1.0–2.5 eV), as shown in Figure 7b. For these compounds, the VBMs predominately feature S/Se p states, and the CBMs contain transition metal d states. It was found that the hexagonal and needle-like phases are not suitable for thin-film solar cells due to their small or pseudo-direct bandgaps. The distorted perovskites, such as $CaTiS_3$, $BaZrS_3$, $CaZrSe_3$, and $CaHfSe_3$, have been proposed to be good PV materials due to their appropriate bandgaps and high optical absorptions, which are comparable to traditional PV materials, such as Si, GaAs, CdTe, and $CuInSe_2$. Additionally, the dispersive band edges and low effective masses in Zr and Hf-based materials indicate their good transport properties.

A following experiment[156] synthesized some chalcogenide perovskites, including $BaZrS_3$, $CaZrS_3$, $SrTiS_3$, and $SrZrS_3$. XRD measurements indicated that $BaZrS_3$ and $CaZrS_3$ belong to the distorted perovskite phase while $SrTiS_3$ and $SrZrS_3$ adopt the needle-like phase. Ultraviolet (UV)–vis and PL measurements showed that $BaZrS_3$ possesses a direct bandgap of ≈1.73 eV in agreement with the theoretical prediction. In addition, the alloy $BaZr(O_xS_{1-x})_3$ was synthesized, and a widely tunable bandgap from 1.73 to 2.87 eV with varying S concentration was observed. Two other recent experiments have reported the bandgap of $BaZrS_3$ to be between 1.83 and 1.85 eV.[157,158] This small discrepancy requires further experiments to resolve.

Meng et al. studied the alloy and defect properties of $BaZrS_3$ based on DFT calculations.[158] They investigated the alloy $BaZrS_3$ with Ti at the Zr sites and Se at the S sites. Calculations showed a relatively dispersive band edge and reduced bandgap with high optical absorption. Defect calculations revealed that, at moderate (near stoichiometric) synthesis condition, deep-level defects and excessively high carrier density

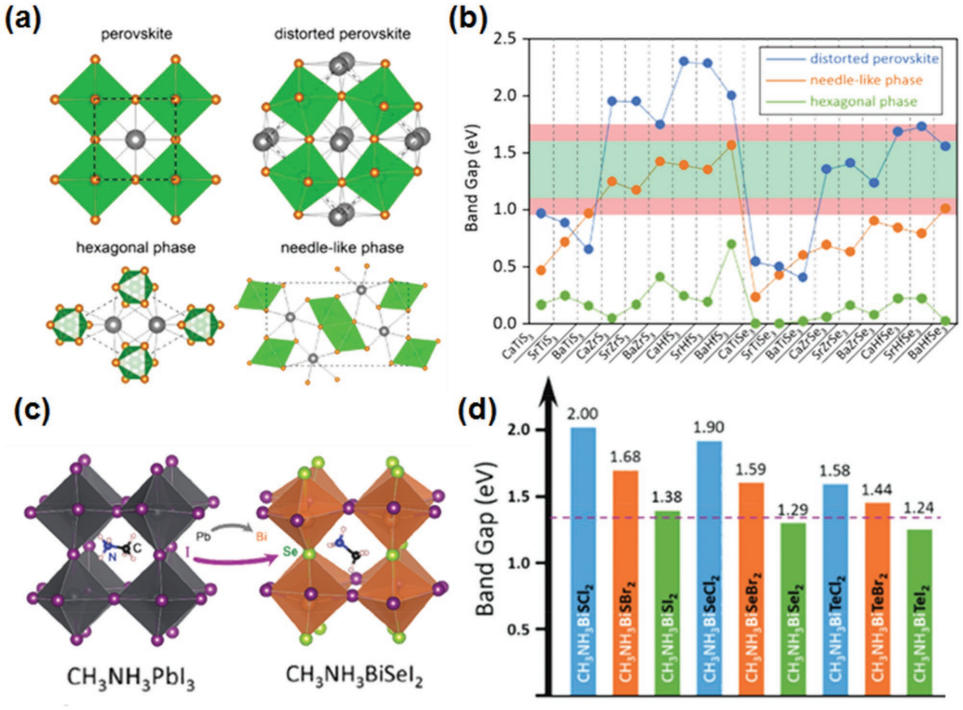

Figure 7. a) Different phases for ABX_3 compounds: ideal perovskite phase without distortion, distorted perovskite phase with a Pnma space group, hexagonal phase with a $P6_3/mmc$ space group, and needle-like phase with a Pnma space group. b) Bandgaps of 18 ABX_3 compounds in distorted perovskite, needle-like, and hexagonal phases calculated by the HSE functional. The optimal bandgap region for solar-cell application is highlighted in light green. The light red region shows an extended optimal region. a,b) Reproduced with permission.[153] Copyright 2015, American Chemical Society. c) Atomic structures of $CH_3NH_3PbI_3$ and $CH_3NH_3BiSeI_2$ and a schematic illustrating the split-anion approach to replace Pb in $CH_3NH_3PbI_3$. d) Calculated bandgaps of $CH_3NH_3BiXY_2$ compounds (with X = S, Se, or Te and Y = Cl, Br, or I) using the HSE functional with SOC. The dashed line marks the optimal bandgap for a single-junction solar cell according to the Shockley–Queisser theory. c,d) Reproduced with permission.[154] Copyright 2016, Royal Society of Chemistry.

can be prevented. Additionally, $BaZrS_3$ perovskites with ambipolar self-doping properties may form homojunctions under proper growth conditions. Unfortunately, both calculations and experiments suggested that $BaZr_{1-x}Ti_xS_3$ thin films might be unstable. It has been suggested that introducing compressive strain may improve the stability. Recent Raman and optical measurements on $BaZrS_3$ under high pressure up to 8 GPa suggested that $BaZrS_3$ could sustain high pressure without changing the perovskite structure and that the bandgap could be reduced with reduced lattice constants.[159]

Recently, Niu et al. synthesized $BaZrS_3$ (BZS) in a perovskite phase and $SrZrS_3$ (SZS) in both a needle-like phase (α-SZS) and distorted perovskite phase (β-SZS).[157] PL spectroscopy showed direct bandgaps of 1.53, 2.13, and 1.81 eV for α-SZS, β-SZS, and BZS, respectively. β-SZS and BZS showed high optical absorption coefficients ($\approx 2 \times 10^5$ cm^{-1} in the visible region), while α-SZS showed much weaker absorption in this region, suggesting a pseudo-direct gap.

Ju et al. investigated a series of Sn/Ge-based chalcogenide perovskites ABX_3, where A = Ca, Sr, or Ba, B = Sn, Ge, or Te, and X = S, Se, or O with distorted perovskite structures based on DFT calculations.[160] Eight compounds showed bandgaps within the optimal range. Four of them, $SrSnS_3$ (1.56 eV), $SrSnSe_3$ (1.00 eV), $CaSnS_3$ (1.58 eV), and $CaGeO_3$ (1.15 eV), showed direct bandgaps. $SrSnS_3$, $SrSnSe_3$, and $CaSnS_3$ showed high absorption in the visible region, with $SrSnSe_3$ displaying similar absorption as $MAPbI_3$. Meanwhile, $SrSnSe_3$ and $SrSnS_3$ with relatively small effective masses were predicted to possess good carrier transport properties.

To explore more lead-free alternatives for hybrid lead perovskites, a split-anion approach to replacing Pb in $CH_3NH_3PbI_3$ with the nontoxic element Bi was proposed, leading to I–III–VI–VII_2 compounds.[154] The approach was inspired by the widely adopted split-cation approach that yields CdTe, $CuInSe_2$, and Cu_2ZnSnS_4, which are all derived from the diamond structure. By substituting one I per formula with S or Se, Pb can be replaced by Bi while maintaining charge neutrality or stoichiometry, as shown in Figure 7c. According to the calculations, both $CH_3NH_3BiSI_2$ and $CH_3NH_3BiSeI_2$ showed direct bandgaps with optimal solar-absorber values of 1.3–1.4 eV, as shown in Figure 7d. The electronic structures of the split-anion materials were found to be similar to that of $CH_3NH_3PbI_3$, except that the S 3p states contribute to the VBM and that the Bi 6p states contribute to the CBM of $CH_3NH_3BiSI_2$. According to DFT-PBE calculations, the effective masses of the electrons and holes are comparable to but slightly larger than those of $CH_3NH_3PbI_3$. $CH_3NH_3BiSI_2$ showed stronger optical absorption than $CH_3NH_3PbI_3$ below 3 eV, which is promising for PV application. Hong et al. also studied $AB(Ch,X)_3$ compounds (A = Cs or Ba; B = Sb or Bi; Ch = chalcogen; X = halogen) based on DFT calculations and solid-state reaction. They showed that these quaternary perovskites are thermodynamically unstable and tend to decompose to binary and ternary compounds or nonperovskite structures.[161]

3.2. Ferroelectric Oxide Perovskites

Ferroelectric oxide perovskites have been widely studied for PV applications owing to the special ferroelectric PV effect. In contrast to conventional PV devices, which rely on p–n junctions to separate electrons and holes, ferroelectric PV materials exhibit spontaneous polarization, which can generate an electric field to separate carriers. This is sometimes called the bulk PV effect. Under illumination, ferroelectric PV materials can produce photocurrent parallel to the polarization direction and open-circuit voltage exceeding the bandgap of the ferroelectric material.[162,163] Moreover, the bulk PV effect may lead to the PCE of the ferroelectric PV device exceeding the Shockley–Queisser limit.

The traditional ferroelectric oxide perovskites usually have wide bandgaps resulting from the large electronegativity difference between the B-site elements and oxygen, which contributes to the CBM and VBM, respectively. Typically, oxide perovskites have bandgaps larger than 3 eV and absorb sunlight in the UV region only. This will limit the application of ferroelectric PV devices. Therefore, significant efforts have been devoted to reducing the bandgap while maintaining the ferroelectricity. Next, we briefly review several of such efforts toward this goal.

For Pb-based ferroelectric perovskite $PbTiO_3$, based on first-principles DFT-based calculations, Rappe et al. partially substituted the B-site Ti with d^8 M^{2+} transition metals (Ni, Pd, or Pt), whose bonding with oxygen is less ionic, while inducing oxygen vacancies to stabilize the structure. Solid solutions with compositions of $Pb(Ti_{1-x}M_x)O_{3-\delta}$ exhibit reduced bandgaps with the polarization preserved or even enhanced, as shown in **Figure 8**c.[164,168] A similar approach was applied to the Pb-free ferroelectric perovskite $BaTiO_3$.[169] However, these materials with a high concentration of O vacancies will hinder the polarization switchable responses and lead to recombination of photogenerated carriers. By investigating highly tetragonal ferroelectric solid solutions of $Bi(Zn_xM_{1-x})O_3$ with M = Ti, W, or Mo, it was found that B-site ordering, structural tetragonality (c/a), and oxygen octahedron tilting can affect the band-edge positions, and the bandgap with an extreme tetragonal structure is highly sensitive to the B-cation ordering and oxygen octahedron tilting.[170] In addition, layered B-site arrangement results in a small bandgap and potentially high electron mobility, which is comparable to those of Si and other classic semiconductors.

Another development was based on $KNbO_3$. A complex substitution scheme resulted in a $75\%KNbO_3$–$25\%(Sr_{1/2}La_{1/2})(Zn_{1/2}Nb_{1/2})O_3$ solid solution, which has a bandgap of 2.1 eV. Under strain, the gap can be further reduced through polarization rotation, as shown in Figure 8d.[165] This strategy was experimentally attempted to introduce two metals into the B sites, where Nb ensures the polarization and other elements, such as Ni^{2+}, accompanied by O vacancies tune the bandgap to the visible region. The resultant $[KNbO_3]_{1-x}[BaNi_{1/2}Nb_{1/2}]O_{3-\delta}$ (KBNNO) solid solutions exhibited ferroelectricity and a widely varying bandgap from 1.1 to 3.8 eV. Particularly, when $x = 0.1$, the material exhibited a direct bandgap of 1.39 eV with polarization and a generated photocurrent density larger than those of traditional ferroelectric oxide perovskites, as shown in Figure 8e.[166] In addition to substitution, other strategies have been employed to tailor the bandgap. It was found that a structural transition from the rhombohedral to tetragonal phase induces polarization rotation, which can reduce the bandgap by up to 1.2 eV due to the effect of BO_6 octahedron distortion.[171]

The multiferroic oxide perovskite $BiFeO_3$ with a smaller bandgap of 2.67 eV and large polarization has also received

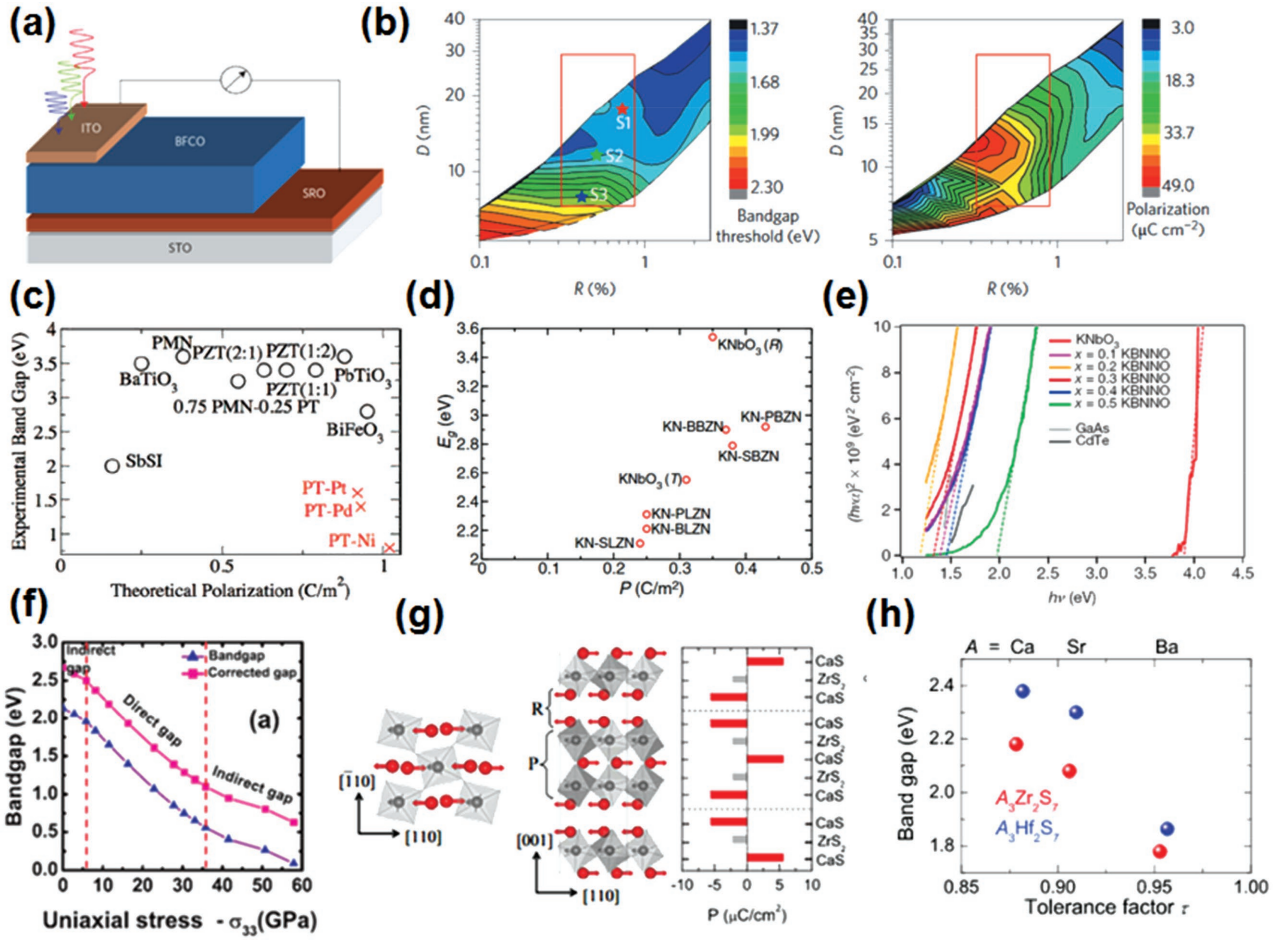

Figure 8. a) Schematic of a BFCO-based single-layer ferroelectric PV device. b) Mappings of the bandgap threshold and ferroelectric polarization with ordering characteristics R and D in the BFCO films. a,b) Reproduced with permission.[56] Copyright 2015, Nature Publishing Group. c) Experimentally measured bandgaps of ferroelectrics versus their theoretical polarizations. The only ferroelectrics with a bandgap of ≈2 eV are SbSI and related compounds. The × signs mark the estimated values for the materials of $PbTiO_3$ doped with Pt, Pd, and Ni (Note the high $\vec{P}$ and low E_{gap}). Reproduced with permission.[164] Copyright 2008, American Chemical Society. d) The HSE bandgaps as a function of the polarization for the designed solid solutions in fully relaxed configurations, including different $KNbO_3$-based solid solutions. Both rhombohedral (R) and tetragonal (T) $KNbO_3$ are shown for comparison. Reproduced with permission.[165] Copyright 2014, APS. e) Ellipsometry measurements for KBNNO oxides with $x = 0.0$–0.5, showing bandgaps from 1.18 to 3.8 eV. This makes KBNNO promising for visible-light absorption. Reproduced with permission.[166] Copyright 2013, AIP Publishing. f) Bandgap as a function of the uniaxial stress ($-\sigma_{33}$) with and without a scissor shift of the bandgaps by 0.54 eV (shifted data are indicated as corrected gap). Reproduced with permission.[167] Copyright 2013, AIP Publishing. g) Crystal structure of Ruddlesden–Popper $A_3B_2S_7$ with orthorhombic $A2_1am$ symmetry. A top view of the perovskite (P) block and side views of both the perovskite and rock-salt (R) blocks in $A_3B_2S_7$ are presented. Cation displacement is shown as arrows. The polarization in each layer is shown on the right panel, which results in a nonzero net polarization. h) HSE-predicted bandgaps for Ruddlesden–Popper $A_3B_2S_7$ sorted by the perovskite tolerance factor. g,h) Reproduced with permission.[173] Copyright 2016, Elsevier.

intensive attention. Through DFT study of the effect of uniaxial compression and biaxial tension, Dong et al. found that the bandgap of rhombohedral $BiFeO_3$ can be reduced to the ideal value of 1.34 eV for PV applications. Moreover, in this process, the bandgap is transformed from indirect to direct leading to an enhanced optical absorption, as shown in Figure 8f.[167] Recently, Nechache et al. investigated the multiferroic material Bi_2FeCrO_6 (BFCO). By tuning the Fe/Cr cationic ordering and the size of the ordered domain, the bandgap was reduced to 1.4 eV. A PCE of 3.3% was achieved for a single-layer solar cell. For multilayer cells, an impressive PCE as high as 8.1% was achieved, as shown in Figure 8a,b.[56]

Generally, when narrowing the bandgap of a ferroelectric perovskite through a bulk approach, the polarization is also reduced substantially. Recently, Matsuo et al. reported an approach to enhance the ferroelectric PV effect. They introduced half-filled defect states in the bandgap. Under illumination, the half-filled defect states serving as stepping stones enabled the empty states to receive electrons from the VB and the filled states to supply electrons to the CB. An experiment using $BiFeO_3$ demonstrated that this strategy can improve not only the photocurrent but also the photovoltage, which is different from intermediate-band solar cells. The approach opens a promising route for the material design of visible-light-absorbing ferroelectrics without sacrificing spontaneous polarization.[172]

Another strategy of reducing the bandgap of a ferroelectric material is to consider chalcogenide ferroelectric materials. Wang et al. found that the Ruddlesden–Popper $A_3B_2S_7$ chalcogenide perovskites possess ferroelectricity. $Ba_3Zr_2S_7$ with a small bandgap of ≈1.8 eV was found to exhibit weak ferroelectric polarization. By replacing Ba with Ca, the ferroelectric polarization was significantly enhanced albeit at the expense of an increased bandgap to 2.2 eV, as shown in Figure 8g,h. The potential of chalcogenide ferroelectrics is worth further investigations.[173]

4. Conclusion and Perspective

We have highlighted the recent theoretical and experimental progress on the materials design of perovskite-solar-cell materials by tailoring the composition and stoichiometry. Most of these efforts have been aimed at addressing two key challenges, that is, the stability and toxicity of lead halide perovskites, which currently limit their commercial application. Toward this goal, chemical composition engineering through alloying at different structural sites has been extensively carried out by experiments. Meanwhile, high-throughput studies based on first-principles calculations have become a main thrust in accelerating this materials design process. Such computational works have played instrumental roles in screening the huge library of possible compositions, especially in predicting their stable phases and PV-related properties, such as bandgaps, optical absorptions, and carrier transport and defect properties.

Materials design has been conducted for both isovalent and heterovalent substitutions of the current lead halide perovskites. The heterovalent substitutions with the constraint of a preserved stoichiometry provide significantly larger compositional space, where high-throughput computational screening manifests its advantages. Heterovalent substitution of I-Pb-VII_3 for lead-free perovskites can be classified into three categories: (i) cation-splitting, where two formula units of $A^{1+}M^{2+}X^{1-}{}_3$ are substituted into $A^{1+}{}_2M^{1+}M'^{3+}X^{1-}{}_6$ (i.e., double perovskites); (ii) cosubstitution of both cations and anions, where (in chalcogenide perovskites) the anions are completely replaced with chalcogens, allowing more choices on the substitution at the B-site cations to replace Pb; (iii) ordered-vacancy perovskites, where two formula units of $A^{1+}M^{2+}X^{1-}{}_3$ are substituted into $A^{1+}{}_2M^{4+}V^0X^{1-}{}_6$ or three formula units are substituted into $A^{1+}{}_3M^{3+}M'^{3+}V^0X^{1-}{}_9$, etc. Here, V^0 represents a vacancy. Through such classification, one can realize other possibilities. For instance, partially replacing the halide anions, for example, $A^{1+}M^{3+}X^{2-}Y^{1-}{}_2$ or $A^{1+}M^{4+}X^{2-}{}_2Y^{1-}$, is possible. Ordered-vacancy perovskites based on more than three formula units are also worth exploring.

In addition to composition engineering, the Ruddlesden–Popper phase represents an important class of perovskite-derived materials. Reducing the dimensions from 3D to quasi-2D has been shown to be a promising strategy to improve the stability while preserving the PV properties, such as carrier mobility, to realize an attractive solar-cell performance. Thus far, studies on the Ruddlesden–Popper phase have been mainly conducted on lead halides. It is of great interest to extend such studies to other perovskites, such as those discussed in the previous paragraph.

Most of the design approaches above have also been applied to ferroelectric oxide perovskites. For PV applications, efforts have been devoted to reducing the bandgap while maintaining the polarization. Introducing defect states within the bandgap has appeared as a promising route for the design of ferroelectric PV materials. This modification can improve not only the photocurrent but also the photovoltage without sacrificing spontaneous polarization. To date, ferroelectric PV devices with significantly improved device efficiency are still to be demonstrated.

Acknowledgements

Q.X. and D.Y. contributed equally to this work. The authors acknowledge funding support from the National Natural Science Foundation of China under Grant Nos. 61722403, 11674121, and 11774365, National Key Research and Development Program of China (under Grants No. 2016YFB0201204), the Recruitment Program of Global Youth Experts in China, the Program for JLU Science and Technology Innovative Research Team, and the Special Fund for Talent Exploitation in Jilin Province of China.

Conflict of Interest

The authors declare no conflict of interest.

Keywords

hybrid halide perovskites, materials by design, photovoltaic absorbers, solar cells

Received: September 30, 2017
Revised: November 26, 2017
Published online:

[1] I. PVPS, *IEA Photovolt. Power Syst. Programme Rep. T1-29*. **2017**.
[2] M. A. Green, A. Ho-Baillie, H. J. Snaith, *Nat. Photonics* **2014**, *8*, 506.
[3] S. Yun, X. Zhou, J. Even, A. Hagfeldt, *Angew. Chem., Int. Ed.* **2017**, *56*, 2.
[4] Z. Xiao, Y. Yan, *Adv. Energy Mater.* **2017**, *7*, 1701136.
[5] M. A. Green, A. Ho-Baillie, *ACS Energy Lett.* **2017**, *2*, 822.
[6] Z. Fan, K. Sun, J. Wang, *J. Mater. Chem. A* **2015**, *3*, 18809.
[7] B. Saparov, D. B. Mitzi, *Chem. Rev.* **2016**, *116*, 4558.
[8] H. Hu, B. Dong, W. Zhang, *J. Mater. Chem. A* **2017**, *5*, 11436.
[9] J. S. Manser, J. A. Christians, P. V. Kamat, *Chem. Rev.* **2016**, *116*, 12956.
[10] W.-J. Yin, J.-H. Yang, J. Kang, Y. Yan, S.-H. Wei, *J. Mater. Chem. A* **2015**, *3*, 8926.
[11] A. M. Ganose, C. N. Savory, D. O. Scanlon, *Chem. Commun.* **2017**, *53*, 20.
[12] K. T. Butler, J. M. Frost, A. Walsh, *Energy Environ. Sci.* **2015**, *8*, 838.
[13] M. A. Jalaja, S. Dutta, *Adv. Mater. Lett.* **2015**, *6*, 568.
[14] C. Paillard, X. Bai, I. C. Infante, M. Guennou, G. Geneste, M. Alexe, J. Kreisel, B. Dkhil, *Adv. Mater.* **2016**, *28*, 5153.
[15] M. Saliba, T. Matsui, K. Domanski, J.-Y. Seo, A. Ummadisingu, S. M. Zakeeruddin, J.-P. Correa-Baena, W. R. Tress, A. Abate, A. Hagfeldt, M. Grätzel, *Science* **2016**, *354*, 206.

[16] NREL, https://www.nrel.gov/pv/assets/images/efficiency-chart.png (accessed: October 2017).
[17] Z. Li, M. Yang, J.-S. Park, S.-H. Wei, J. J. Berry, K. Zhu, *Chem. Mater.* **2016**, *28*, 284.
[18] H. Zhang, H. Wang, S. T. Williams, D. Xiong, W. Zhang, C.-C. Chueh, W. Chen, A. K.-Y. Jen, *Adv. Mater.* **2017**, *29*, 1606608.
[19] L. Li, N. Liu, Z. Xu, Q. Chen, X. Wang, H. Zhou, *ACS Nano* **2017**, *11*, 8804.
[20] N. Pellet, P. Gao, G. Gregori, T.-Y. Yang, M. K. Nazeeruddin, J. Maier, M. Grätzel, *Angew. Chem., Int. Ed.* **2014**, *53*, 3151.
[21] M. M. Lee, J. Teuscher, T. Miyasaka, T. N. Murakami, H. J. Snaith, *Science* **2012**, *338*, 643.
[22] J. H. Noh, S. H. Im, J. H. Heo, T. N. Mandal, S. I. Seok, *Nano Lett.* **2013**, *13*, 1764.
[23] Y. Ogomi, A. Morita, S. Tsukamoto, T. Saitho, N. Fujikawa, Q. Shen, T. Toyoda, K. Yoshino, S. S. Pandey, T. Ma, S. Hayase, *J. Phys. Chem. Lett.* **2014**, *5*, 1004.
[24] M. Saliba, T. Matsui, J.-Y. Seo, K. Domanski, J.-P. Correa-Baena, M. K. Nazeeruddin, S. M. Zakeeruddin, W. Tress, A. Abate, A. Hagfeldt, M. Grätzel, *Energy Environ. Sci.* **2016**, *9*, 1989.
[25] Y. Li, W. Sun, W. Yan, S. Ye, H. Rao, H. Peng, Z. Zhao, Z. Bian, Z. Liu, H. Zhou, C. Huang, *Adv. Energy Mater.* **2016**, *6*, 1601353.
[26] A. H. Slavney, T. Hu, A. M. Lindenberg, H. I. Karunadasa, *J. Am. Chem. Soc.* **2016**, *138*, 2138.
[27] G. Volonakis, M. R. Filip, A. A. Haghighirad, N. Sakai, B. Wenger, H. J. Snaith, F. Giustino, *J. Phys. Chem. Lett.* **2016**, *7*, 1254.
[28] H. Tsai, W. Nie, J.-C. Blancon, C. C. Stoumpos, R. Asadpour, B. Harutyunyan, A. J. Neukirch, R. Verduzco, J. J. Crochet, S. Tretiak, L. Pedesseau, J. Even, M. A. Alam, G. Gupta, J. Lou, P. M. Ajayan, M. J. Bedzyk, M. G. Kanatzidis, A. D. Mohite, *Nature* **2016**, *536*, 312.
[29] L. N. Quan, M. Yuan, R. Comin, O. Voznyy, E. M. Beauregard, S. Hoogland, A. Buin, A. R. Kirmani, K. Zhao, A. Amassian, D. H. Kim, E. H. Sargent, *J. Am. Chem. Soc.* **2016**, *138*, 2649.
[30] B. Saparov, F. Hong, J.-P. Sun, H.-S. Duan, W. Meng, S. Cameron, I. G. Hill, Y. Yan, D. B. Mitzi, *Chem. Mater.* **2015**, *27*, 5622.
[31] Z. Zhang, X. Li, X. Xia, Z. Wang, Z. Huang, B. Lei, Y. Gao, *J. Phys. Chem. Lett.* **2017**, *8*, 4300.
[32] M. Grätzel, *Nat. Mater.* **2014**, *13*, 838.
[33] A. Poglitsch, D. Weber, *J. Chem. Phys.* **1987**, *87*, 6373.
[34] D. Weber, *Z. Naturforsch., B: J. Chem. Sci.* **1978**, *33*, 1443.
[35] T. Umebayashi, K. Asai, T. Kondo, A. Nakao, *Phys. Rev. B* **2003**, *67*, 155405.
[36] Y. H. Chang, C. H. Park, K. Matsuishi, *J. Korean Phys. Soc.* **2004**, *44*, 889.
[37] N. J. Jeon, J. H. Noh, Y. C. Kim, W. S. Yang, S. Ryu, S. I. Seok, *Nat. Mater.* **2014**, *13*, 897.
[38] J. P. C. Baena, L. Steier, W. Tress, M. Saliba, S. Neutzner, T. Matsui, F. Giordano, T. J. Jacobsson, A. R. S. Kandada, S. M. Zakeeruddin, A. Petrozza, A. Abate, M. K. Nazeeruddin, M. Grätzel, A. Hagfeldt, *Energy Environ. Sci.* **2015**, *8*, 2928.
[39] F. Bella, G. Griffini, J.-P. Correa-Baena, G. Saracco, M. Grätzel, A. Hagfeldt, S. Turri, C. Gerbaldi, *Science* **2016**, https://doi.org/10.1126/science.aah4046.
[40] T. Leijtens, G. E. Eperon, S. Pathak, A. Abate, M. M. Lee, H. J. Snaith, *Nat. Commun.* **2013**, *4*, 2885.
[41] A. H. Slavney, R. W. Smaha, I. C. Smith, A. Jaffe, D. Umeyama, H. I. Karunadasa, *Inorg. Chem.* **2017**, *56*, 46.
[42] J.-W. Lee, D.-H. Kim, H.-S. Kim, S.-W. Seo, S. M. Cho, N.-G. Park, *Adv. Energy Mater.* **2015**, *5*, 1501310.
[43] H.-S. Kim, C.-R. Lee, J.-H. Im, K.-B. Lee, T. Moehl, A. Marchioro, S.-J. Moon, R. Humphry-Baker, J.-H. Yum, J. E. Moser, M. Grätzel, N.-G. Park, *Sci. Rep.* **2012**, *2*, 591.
[44] I. C. Smith, E. T. Hoke, D. Solis-Ibarra, M. D. McGehee, H. I. Karunadasa, *Angew. Chem., Int. Ed.* **2014**, *53*, 11232.
[45] X. Zhang, X. Ren, B. Liu, R. Munir, X. Zhu, D. Yang, J. Li, Y. Liu, D.-M. Smilgies, R. Li, Z. Yang, T. Niu, X. Wang, A. Amassian, K. Zhao, S. (F.) Liu, *Energy Environ. Sci.* **2017**, *10*, 2095.
[46] B.-W. Park, B. Philippe, X. Zhang, H. Rensmo, G. Boschloo, E. M. J. Johansson, *Adv. Mater.* **2015**, *27*, 6806.
[47] A. Kojima, K. Teshima, Y. Shirai, T. Miyasaka, *J. Am. Chem. Soc.* **2009**, *131*, 6050.
[48] E. Greul, M. L. Petrus, A. Binek, P. Docampo, T. Bein, *J. Mater. Chem. A* **2017**, *5*, 19972.
[49] D. H. Cao, C. C. Stoumpos, O. K. Farha, J. T. Hupp, M. G. Kanatzidis, *J. Am. Chem. Soc.* **2015**, *137*, 7843.
[50] K. Yao, X. Wang, Y. Xu, F. Li, L. Zhou, *Chem. Mater.* **2016**, *28*, 3131.
[51] X. Zhang, G. Wu, S. Yang, W. Fu, Z. Zhang, C. Chen, W. Liu, J. Yan, W. Yang, H. Chen, *Small* **2017**, *13*, 1700611.
[52] J.-C. Hebig, I. Kühn, J. Flohre, T. Kirchartz, *ACS Energy Lett.* **2016**, *1*, 309.
[53] C. Zuo, L. Ding, *Angew. Chem., Int. Ed.* **2017**, *56*, 6528.
[54] P. C. Harikesh, H. K. Mulmudi, B. Ghosh, T. W. Goh, Y. T. Teng, K. Thirumal, M. Lockrey, K. Weber, T. M. Koh, S. Li, S. Mhaisalkar, N. Mathews, *Chem. Mater.* **2016**, *28*, 7496.
[55] X. Qiu, B. Cao, S. Yuan, X. Chen, Z. Qiu, Y. Jiang, Q. Ye, H. Wang, H. Zeng, J. Liu, M. G. Kanatzidis, *Sol. Energy Mater. Sol. Cells* **2017**, *159*, 227.
[56] R. Nechache, C. Harnagea, S. Li, L. Cardenas, W. Huang, J. Chakrabartty, F. Rosei, *Nat. Photonics* **2015**, *9*, 61.
[57] F. Zheng, Y. Xin, W. Huang, J. Zhang, X. Wang, M. Shen, W. Dong, L. Fang, Y. Bai, X. Shen, J. Hao, *J. Mater. Chem. A* **2014**, *2*, 1363.
[58] C. C. Stoumpos, C. D. Malliakas, M. G. Kanatzidis, *Inorg. Chem.* **2013**, *52*, 9019.
[59] K. Tanaka, T. Takahashi, T. Ban, T. Kondo, K. Uchida, N. Miura, *Solid State Commun.* **2003**, *127*, 619.
[60] A. Miyata, A. Mitioglu, P. Plochocka, O. Portugall, J. T.-W. Wang, S. D. Stranks, H. J. Snaith, R. J. Nicholas, *Nat. Phys.* **2015**, *11*, 582.
[61] K. Galkowski, A. Mitioglu, A. Miyata, P. Plochocka, O. Portugall, G. E. Eperon, J. T.-W. Wang, T. Stergiopoulos, S. D. Stranks, H. J. Snaith, R. J. Nicholas, *Energy Environ. Sci.* **2016**, *9*, 962.
[62] S. D. Stranks, G. E. Eperon, G. Grancini, C. Menelaou, M. J. P. Alcocer, T. Leijtens, L. M. Herz, A. Petrozza, H. J. Snaith, *Science* **2013**, *342*, 341.
[63] M. B. Johnston, L. M. Herz, *Acc. Chem. Res.* **2016**, *49*, 146.
[64] W. S. Yang, B.-W. Park, E. H. Jung, N. J. Jeon, Y. C. Kim, D. U. Lee, S. S. Shin, J. Seo, E. K. Kim, J. H. Noh, S. I. Seok, *Science* **2017**, *356*, 1376.
[65] L. Cai, L. Liang, J. Wu, B. Ding, L. Gao, B. Fan, *J. Semicond.* **2017**, *38*, 014006.
[66] J. Borchert, R. L. Milot, J. B. Patel, C. L. Davies, A. D. Wright, L. M. Maestro, H. J. Snaith, L. M. Herz, M. B. Johnston, *ACS Energy Lett.* **2017**, *2*, 2799.
[67] W.-J. Yin, T. Shi, Y. Yan, *Appl. Phys. Lett.* **2014**, *104*, 063903.
[68] F. Brivio, A. B. Walker, A. Walsh, *APL Mater.* **2013**, *1*, 042111.
[69] W.-J. Yin, T. Shi, Y. Yan, *Adv. Mater.* **2014**, *26*, 4653.
[70] D. P. McMeekin, G. Sadoughi, W. Rehman, G. E. Eperon, M. Saliba, M. T. Hörantner, A. Haghighirad, N. Sakai, L. Korte, B. Rech, M. B. Johnston, L. M. Herz, H. J. Snaith, *Science* **2016**, *351*, 151.
[71] C. Li, X. Lu, W. Ding, L. Feng, Y. Gao, Z. Guo, *Acta Crystallogr., B* **2008**, *64*, 702.
[72] G. E. Eperon, G. M. Paternò, R. J. Sutton, A. Zampetti, A. A. Haghighirad, F. Cacialli, H. J. Snaith, *J. Mater. Chem. A* **2015**, *3*, 19688.
[73] T. Baikie, Y. Fang, J. M. Kadro, M. Schreyer, F. Wei, S. G. Mhaisalkar, M. Graetzel, T. J. White, *J. Mater. Chem. A* **2013**, *1*, 5628.

[74] C. Motta, F. El-Mellouhi, S. Kais, N. Tabet, F. Alharbi, S. Sanvito, *Nat. Commun.* **2015**, *6*, 8026.
[75] F. Zheng, L. Z. Tan, S. Liu, A. M. Rappe, *Nano Lett.* **2015**, *15*, 7794.
[76] H. Zhu, K. Miyata, Y. Fu, J. Wang, P. P. Joshi, D. Niesner, K. W. Williams, S. Jin, X.-Y. Zhu, *Science* **2016**, *353*, 1409.
[77] G. Giorgi, J.-I. Fujisawa, H. Segawa, K. Yamashita, *J. Phys. Chem. Lett.* **2013**, *4*, 4213.
[78] W. Gao, X. Gao, T. A. Abtew, Y.-Y. Sun, S. Zhang, P. Zhang, *Phys. Rev. B* **2016**, *93*, 085202.
[79] B. El Jani, P. Gibart, J. C. Portal, R. L. Aulombard, *J. Appl. Phys.* **1985**, *58*, 3481.
[80] P. Umari, E. Mosconi, F. De Angelis, *Sci. Rep.* **2015**, *4*, 4467.
[81] M. Liu, M. B. Johnston, H. J. Snaith, *Nature* **2013**, *501*, 395.
[82] M. A. Green, K. Emery, Y. Hishikawa, W. Warta, E. D. Dunlop, *Prog. Photovolt. Res. Appl.* **2015**, *23*, 1.
[83] M. H. Du, *J. Mater. Chem. A* **2014**, *2*, 9091.
[84] M. L. Agiorgousis, Y.-Y. Sun, H. Zeng, S. Zhang, *J. Am. Chem. Soc.* **2014**, *136*, 14570.
[85] W. Ming, S. Chen, M.-H. Du, *J. Mater. Chem. A* **2016**, *4*, 16975.
[86] G. Xing, N. Mathews, S. Sun, S. S. Lim, Y. M. Lam, M. Grätzel, S. Mhaisalkar, T. C. Sum, *Science* **2013**, *342*, 344.
[87] F. Giustino, H. J. Snaith, *ACS Energy Lett.* **2016**, *1*, 1233.
[88] S. Chakraborty, W. Xie, N. Mathews, M. Sherburne, R. Ahuja, M. Asta, S. G. Mhaisalkar, *ACS Energy Lett.* **2017**, *2*, 837.
[89] P. V. Kamat, J. Bisquert, J. Buriak, *ACS Energy Lett.* **2017**, *2*, 904.
[90] S. Shukla, S. Shukla, L. J. Haur, S. S. H. Dintakurti, G. Han, A. Priyadarshi, T. Baikie, S. G. Mhaisalkar, N. Mathews, *ChemSusChem* **2017**, *10*, 3804.
[91] E. Edri, S. Kirmayer, M. Kulbak, G. Hodes, D. Cahen, *J. Phys. Chem. Lett.* **2014**, *5*, 429.
[92] K. Cao, H. Li, S. Liu, J. Cui, Y. Shen, M. Wang, *Nanoscale* **2016**, *8*, 8839.
[93] S. Colella, E. Mosconi, P. Fedeli, A. Listorti, F. Gazza, F. Orlandi, P. Ferro, T. Besagni, A. Rizzo, G. Calestani, G. Gigli, F. De Angelis, R. Mosca, *Chem. Mater.* **2013**, *25*, 4613.
[94] B. Suarez, V. Gonzalez-Pedro, T. S. Ripolles, R. S. Sanchez, L. Otero, I. Mora-Sero, *J. Phys. Chem. Lett.* **2014**, *5*, 1628.
[95] W.-J. Yin, Y. Yan, S.-H. Wei, *J. Phys. Chem. Lett.* **2014**, *5*, 3625.
[96] E. Edri, S. Kirmayer, D. Cahen, G. Hodes, *J. Phys. Chem. Lett.* **2013**, *4*, 897.
[97] D. Yang, J. Lv, X. Zhao, Q. Xu, Y. Fu, Y. Zhan, A. Zunger, L. Zhang, *Chem. Mater.* **2017**, *29*, 524.
[98] Q. Jiang, D. Rebollar, J. Gong, E. L. Piacentino, C. Zheng, T. Xu, *Angew. Chem., Int. Ed.* **2015**, *54*, 7617.
[99] S. Nagane, U. Bansode, O. Game, S. Chhatre, S. Ogale, *Chem. Commun.* **2014**, *50*, 9741.
[100] G. E. Eperon, S. D. Stranks, C. Menelaou, M. B. Johnston, L. M. Herz, H. J. Snaith, *Energy Environ. Sci.* **2014**, *7*, 982.
[101] Z. Wang, Y. Zhou, S. Pang, Z. Xiao, J. Zhang, W. Chai, H. Xu, Z. Liu, N. P. Padture, G. Cui, *Chem. Mater.* **2015**, *27*, 7149.
[102] H. Choi, J. Jeong, H.-B. Kim, S. Kim, B. Walker, G.-H. Kim, J. Y. Kim, *Nano Energy* **2014**, *7*, 80.
[103] F. Hao, C. C. Stoumpos, D. H. Cao, R. P. H. Chang, M. G. Kanatzidis, *Nat. Photonics* **2014**, *8*, 489.
[104] W. Liao, D. Zhao, Y. Yu, C. R. Grice, C. Wang, A. J. Cimaroli, P. Schulz, W. Meng, K. Zhu, R.-G. Xiong, Y. Yan, *Adv. Mater.* **2016**, *28*, 9333.
[105] M. R. Filip, F. Giustino, *J. Phys. Chem. C* **2016**, *120*, 166.
[106] A. Kumar, K. R. Balasubramaniam, J. Kangsabanik, Vikram, A. Alam, *Phys. Rev. B* **2016**, *94*, 180105.
[107] T. J. Jacobsson, M. Pazoki, A. Hagfeldt, T. Edvinsson, *J. Phys. Chem. C* **2015**, *119*, 25673.
[108] C. C. Stoumpos, L. Frazer, D. J. Clark, Y. S. Kim, S. H. Rhim, A. J. Freeman, J. B. Ketterson, J. I. Jang, M. G. Kanatzidis, *J. Am. Chem. Soc.* **2015**, *137*, 6804.
[109] W. Ming, H. Shi, M.-H. Du, *J. Mater. Chem. A* **2016**, *4*, 13852.
[110] T. Krishnamoorthy, H. Ding, C. Yan, W. L. Leong, T. Baikie, Z. Zhang, M. Sherburne, S. Li, M. Asta, N. Mathews, S. G. Mhaisalkar, *J. Mater. Chem. A* **2015**, *3*, 23829.
[111] M.-G. Ju, J. Dai, L. Ma, X. C. Zeng, *J. Am. Chem. Soc.* **2017**, *139*, 8038.
[112] N. K. Noel, S. D. Stranks, A. Abate, C. Wehrenfennig, S. Guarnera, A.-A. Haghighirad, A. Sadhanala, G. E. Eperon, S. K. Pathak, M. B. Johnston, A. Petrozza, L. M. Herz, H. J. Snaith, *Energy Environ. Sci.* **2014**, *7*, 3061.
[113] X.-G. Zhao, J.-H. Yang, Y. Fu, D. Yang, Q. Xu, L. Yu, S.-H. Wei, L. Zhang, *J. Am. Chem. Soc.* **2017**, *139*, 2630.
[114] W. Meng, X. Wang, Z. Xiao, J. Wang, D. B. Mitzi, Y. Yan, *J. Phys. Chem. Lett.* **2017**, *8*, 2999.
[115] C. N. Savory, A. Walsh, D. O. Scanlon, *ACS Energy Lett.* **2016**, *1*, 949.
[116] E. T. McClure, M. R. Ball, W. Windl, P. M. Woodward, *Chem. Mater.* **2016**, *28*, 1348.
[117] M. R. Filip, S. Hillman, A. A. Haghighirad, H. J. Snaith, F. Giustino, *J. Phys. Chem. Lett.* **2016**, *7*, 2579.
[118] G. Volonakis, A. A. Haghighirad, H. J. Snaith, F. Giustino, *J. Phys. Chem. Lett.* **2017**, *8*, 3917.
[119] T. T. Tran, J. R. Panella, J. R. Chamorro, J. R. Morey, T. M. McQueen, *Mater. Horiz.* **2017**, *4*, 688.
[120] K. Du, W. Meng, X. Wang, Y. Yan, D. B. Mitzi, *Angew. Chem., Int. Ed.* **2017**, *56*, 8158.
[121] A. H. Slavney, L. Leppert, D. Bartesaghi, A. Gold-Parker, M. F. Toney, T. J. Savenije, J. B. Neaton, H. I. Karunadasa, *J. Am. Chem. Soc.* **2017**, *139*, 5015.
[122] F. Wei, Z. Deng, S. Sun, F. Zhang, D. M. Evans, G. Kieslich, S. Tominaka, M. A. Carpenter, J. Zhang, P. D. Bristowe, A. K. Cheetham, *Chem. Mater.* **2017**, *29*, 1089.
[123] P. Cheng, T. Wu, Y. Li, L. Jiang, W. Deng, K. Han, *New J. Chem.* **2017**, *41*, 9598.
[124] X.-G. Zhao, D. Yang, Y. Sun, T. Li, L. Zhang, L. Yu, A. Zunger, *J. Am. Chem. Soc.* **2017**, *139*, 6718.
[125] G. Volonakis, A. A. Haghighirad, R. L. Milot, W. H. Sio, M. R. Filip, B. Wenger, M. B. Johnston, L. M. Herz, H. J. Snaith, F. Giustino, *J. Phys. Chem. Lett.* **2017**, *8*, 772.
[126] Z. Xiao, K.-Z. Du, W. Meng, D. B. Mitzi, Y. Yan, *Angew. Chem.* **2017**, *129*, 12275.
[127] Z. Xiao, H. Lei, X. Zhang, Y. Zhou, H. Hosono, T. Kamiya, *Bull. Chem. Soc. Jpn.* **2015**, *88*, 1250.
[128] Z. Xiao, Y. Zhou, H. Hosono, T. Kamiya, *Phys. Chem. Chem. Phys.* **2015**, *17*, 18900.
[129] B. Lee, C. C. Stoumpos, N. Zhou, F. Hao, C. Malliakas, C.-Y. Yeh, T. J. Marks, M. G. Kanatzidis, R. P. H. Chang, *J. Am. Chem. Soc.* **2014**, *136*, 15379.
[130] N. Sakai, A. A. Haghighirad, M. R. Filip, P. K. Nayak, S. Nayak, A. Ramadan, Z. Wang, F. Giustino, H. J. Snaith, *J. Am. Chem. Soc.* **2017**, *139*, 6030.
[131] B. Saparov, J.-P. Sun, W. Meng, Z. Xiao, H.-S. Duan, O. Gunawan, D. Shin, I. G. Hill, Y. Yan, D. B. Mitzi, *Chem. Mater.* **2016**, *28*, 2315.
[132] A. E. Maughan, A. M. Ganose, M. M. Bordelon, E. M. Miller, D. O. Scanlon, J. R. Neilson, *J. Am. Chem. Soc.* **2016**, *138*, 8453.
[133] Z. Xiao, W. Meng, J. Wang, D. B. Mitzi, Y. Yan, *Mater. Horiz.* **2016**, *4*, 206.
[134] J.-C. Blancon, H. Tsai, W. Nie, C. C. Stoumpos, L. Pedesseau, C. Katan, M. Kepenekian, C. M. M. Soe, K. Appavoo, M. Y. Sfeir, S. Tretiak, P. M. Ajayan, M. G. Kanatzidis, J. Even, J. J. Crochet, A. D. Mohite, *Science* **2017**, *355*, 1288.
[135] L. Zhang, W. Liang, *J. Phys. Chem. Lett.* **2017**, *8*, 1517.
[136] Q. Shang, Y. Wang, Y. Zhong, Y. Mi, L. Qin, Y. Zhao, X. Qiu, X. Liu, Q. Zhang, *J. Phys. Chem. Lett.* **2017**, *8*, 4431.

[137] Y. Liao, H. Liu, W. Zhou, D. Yang, Y. Shang, Z. Shi, B. Li, X. Jiang, L. Zhang, L. N. Quan, R. Quintero-Bermudez, B. R. Sutherland, Q. Mi, E. H. Sargent, Z. Ning, *J. Am. Chem. Soc.* **2017**, *139*, 6693.
[138] A. Fraccarollo, V. Cantatore, G. Boschetto, L. Marchese, M. Cossi, *J. Chem. Phys.* **2016**, *144*, 164701.
[139] J.-F. Liao, H.-S. Rao, B.-X. Chen, D.-B. Kuang, C.-Y. Su, *J. Mater. Chem. A* **2017**, *5*, 2066.
[140] R. Hamaguchi, M. Yoshizawa-Fujita, T. Miyasaka, H. Kunugita, K. Ema, Y. Takeoka, M. Rikukawa, *Chem. Commun.* **2017**, *53*, 4366.
[141] Y. Liu, H. Xiao, W. A. Goddard, *Nano Lett.* **2016**, *16*, 3335.
[142] L. Ma, J. Dai, X. C. Zeng, *Adv. Energy Mater.* **2017**, *7*, 1601731.
[143] J. Liu, J. Leng, K. Wu, J. Zhang, S. Jin, *J. Am. Chem. Soc.* **2017**, *139*, 1432.
[144] D. H. Cao, C. C. Stoumpos, T. Yokoyama, J. L. Logsdon, T.-B. Song, O. K. Farha, M. R. Wasielewski, J. T. Hupp, M. G. Kanatzidis, *ACS Energy Lett.* **2017**, *2*, 982.
[145] Y. Zhang, J. Yin, M. R. Parida, G. H. Ahmed, J. Pan, O. M. Bakr, J.-L. Brédas, O. F. Mohammed, *J. Phys. Chem. Lett.* **2017**, *8*, 3173.
[146] J. Pal, S. Manna, A. Mondal, S. Das, K. V. Adarsh, A. Nag, *Angew. Chem.* **2017**, *129*, 14375.
[147] M. B. Johansson, H. Zhu, E. M. J. Johansson, *J. Phys. Chem. Lett.* **2016**, *7*, 3467.
[148] Y. Kim, Z. Yang, A. Jain, O. Voznyy, G.-H. Kim, M. Liu, L. N. Quan, F. P. García de Arquer, R. Comin, J. Z. Fan, E. H. Sargent, *Angew. Chem., Int. Ed.* **2016**, *55*, 9586.
[149] H. C. Sansom, G. F. S. Whitehead, M. S. Dyer, M. Zanella, T. D. Manning, M. J. Pitcher, T. J. Whittles, V. R. Dhanak, J. Alaria, J. B. Claridge, M. J. Rosseinsky, *Chem. Mater.* **2017**, *29*, 1538.
[150] Z. Xiao, W. Meng, D. B. Mitzi, Y. Yan, *J. Phys. Chem. Lett.* **2016**, *7*, 3903.
[151] L. F. Mashadieva, Z. S. Aliev, A. V. Shevelkov, M. B. Babanly, *J. Alloys Compd.* **2013**, *551*, 512.
[152] T. Oldag, T. Aussieker, H.-L. Keller, C. Preitschaft, A. Pfitzner, *Z. Anorg. Allg. Chem.* **2005**, *631*, 677.
[153] Y.-Y. Sun, M. L. Agiorgousis, P. Zhang, S. Zhang, *Nano Lett.* **2015**, *15*, 581.
[154] Y.-Y. Sun, J. Shi, J. Lian, W. Gao, M. L. Agiorgousis, P. Zhang, S. Zhang, *Nanoscale* **2016**, *8*, 6284.
[155] R. Lelieveld, D. J. W. IJdo, *Acta Crystallogr., B* **1980**, *36*, 2223.
[156] S. Perera, H. Hui, C. Zhao, H. Xue, F. Sun, C. Deng, N. Gross, C. Milleville, X. Xu, D. F. Watson, B. Weinstein, Y.-Y. Sun, S. Zhang, H. Zeng, *Nano Energy* **2016**, *22*, 129.
[157] S. Niu, H. Huyan, Y. Liu, M. Yeung, K. Ye, L. Blankemeier, T. Orvis, D. Sarkar, D. J. Singh, R. Kapadia, J. Ravichandran, *Adv. Mater.* **2017**, *29*, 1604733.
[158] W. Meng, B. Saparov, F. Hong, J. Wang, D. B. Mitzi, Y. Yan, *Chem. Mater.* **2016**, *28*, 821.
[159] N. Gross, Y.-Y. Sun, S. Perera, H. Hui, X. Wei, S. Zhang, H. Zeng, B. A. Weinstein, *Phys. Rev. Appl.* **2017**, *8*, 044014.
[160] M.-G. Ju, J. Dai, L. Ma, X. C. Zeng, *Adv. Energy Mater.* **2017**, *7*, 1700216.
[161] F. Hong, B. Saparov, W. Meng, Z. Xiao, D. B. Mitzi, Y. Yan, *J. Phys. Chem. C* **2016**, *120*, 6435.
[162] S. Y. Yang, J. Seidel, S. J. Byrnes, P. Shafer, C.-H. Yang, M. D. Rossell, P. Yu, Y.-H. Chu, J. F. Scott, J. W. Ager, L. W. Martin, R. Ramesh, *Nat. Nanotechnol.* **2010**, *5*, 143.
[163] A. Bhatnagar, A. Roy Chaudhuri, Y. H. Kim, D. Hesse, M. Alexe, *Nat. Commun.* **2013**, *4*, 2835.
[164] J. W. Bennett, I. Grinberg, A. M. Rappe, *J. Am. Chem. Soc.* **2008**, *130*, 17409.
[165] F. Wang, I. Grinberg, A. M. Rappe, *Phys. Rev. B* **2014**, *89*, 235105.
[166] I. Grinberg, D. V. West, M. Torres, G. Gou, D. M. Stein, L. Wu, G. Chen, E. M. Gallo, A. R. Akbashev, P. K. Davies, J. E. Spanier, A. M. Rappe, *Nature* **2013**, *503*, 509.
[167] H. Dong, Z. Wu, S. Wang, W. Duan, J. Li, *Appl. Phys. Lett.* **2013**, *102*, 072905.
[168] G. Y. Gou, J. W. Bennett, H. Takenaka, A. M. Rappe, *Phys. Rev. B* **2011**, *83*, 205115.
[169] J. W. Bennett, I. Grinberg, P. K. Davies, A. M. Rappe, *Phys. Rev. B* **2010**, *82*, 184106.
[170] T. Qi, I. Grinberg, A. M. Rappe, *Phys. Rev. B* **2011**, *83*, 224108.
[171] F. Wang, I. Grinberg, A. M. Rappe, *Appl. Phys. Lett.* **2014**, *104*, 152903.
[172] H. Matsuo, Y. Noguchi, M. Miyayama, *Nat. Commun.* **2017**, *8*,207.
[173] H. Wang, G. Gou, J. Li, *Nano Energy* **2016**, *22*, 507.